Development of unsteady natural convection in a square cavity under large temperature difference

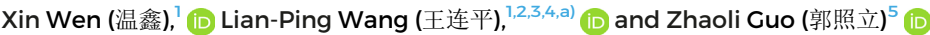
Cite as: Phys. Fluids **33**, 084108 (2021); doi: 10.1063/5.0058399 Submitted: 29 May 2021 · Accepted: 28 July 2021 ·

Published Online: 16 August 2021













- ¹126 Spencer Laboratory, Department of Mechanical Engineering, University of Delaware, Newark, Delaware 19716-3140, USA
- 2 Guangdong Provincial Key Laboratory of Turbulence Research and Applications, Center for Complex Flows and Soft Matter Research and Department of Mechanics and Aerospace Engineering, Southern University of Science and Technology, Shenzhen 518055, Guangdong, China
- ³Southern Marine Science and Engineering Guangdong Laboratory (Guangzhou), Guangzhou 511458, China
- ⁴Guangdong-Hong Kong-Macao Joint Laboratory for Data-Driven Fluid Mechanics and Engineering Applications, Southern University of Science and Technology, Shenzhen 518055, China
- 5 State Key Laboratory of Coal Combustion, School of Energy and Power Engineering, Huazhong University of Science and Technology, Wuhan 430074, Hubei, China

ABSTRACT

To investigate how the nonuniform fluid density distribution caused by large temperature variations affects the development of unsteady natural convection, we perform a series of direct numerical simulations of two-dimensional compressible natural convection in an air-filled square cavity. The cavity has a hot wall on the left and a cold wall on the right, and two horizontal walls are adiabatic. The simulations are done using a kinetic approach based on a modeled Boltzmann equation, from which the fully compressible Navier-Stokes-Fourier equations are recovered. No Boussinesq approximation or low Mach number approximation is made. An extra source term is introduced to adjust the fluid Prandtl number. Simulations are performed for a range of Rayleigh numbers $(10^7 - 10^9)$ with a fixed dimensionless temperature difference of $\varepsilon = 0.6$ to determine the critical Rayleigh number and study the development of unsteady flow. To illustrate the instability mechanism, instantaneous fluctuation field, time trace of temperature, and velocity at selected monitoring points, the spectrum and other statistics are presented and discussed. As expected, significant differences are observed between the instability of compressible natural convection and the Boussinesq-type natural convection. With a large temperature difference, the transition to unsteady flow is asymmetric for the flows near the hot wall and cold wall. For the Rayleigh number range we studied, the cold wall region is dominated by low-frequency impact instability of the boundary thermal jet at the bottom corner. For the hot wall region, besides the upper corner impact instability, a boundary layer instability featuring high-frequency oscillations is observed.

Published under an exclusive license by AIP Publishing. https://doi.org/10.1063/5.0058399

I. INTRODUCTION

Natural convection in an enclosure has been investigated by researchers from various perspectives for decades. 1-4 The instability mechanism of the flow is a crucial topic of convection flows.⁵ The onset of unsteady flow can be affected by a large range of system parameters, such as aspect ratio, Prandtl number, applied temperature difference, etc. 6-8 Based on the applied temperature difference $\varepsilon = (T_h - T_c)/(T_h + T_c)$, the buoyancy-driven natural convection can be classified into two types: (1) When the temperature difference is small such that the flow can be assumed to be nearly incompressible and the buoyancy effect can be related to a linear function of local

temperature, namely, the Boussinesq approximation. Under the Boussinesq approximation, the fluid properties such as viscosity ν and heat conductivity κ are treated as constants. The work done by viscous dissipation and compression can be neglected. (2) For a large temperature difference, the flow becomes compressible and the fluid density variation must be considered. The momentum equation and the energy equation are strongly coupled. The flow is now governed by fully compressible Navier-Stokes equations. The knowledge of Boussinesq-type natural convection is now relatively complete as it has been studied by researchers using different numerical methods; flow transition and structures at different Rayleigh numbers have been

^{a)}Author to whom correspondence should be addressed: wanglp@sustech.edu.cn

examined. $^{9-11}$ However, the instability mechanism of compressible natural convection in an enclosure is largely unexplored. In this paper, we focus specifically on the unsteady compressible natural convection in an air-filled (Pr=0.71) square cavity with differentially heated vertical walls (DHVW). Two horizontal walls are adiabatic. A summary of previous numerical studies relevant to the instability mechanism of this second type of natural convection in a cavity with DHVW is presented in the following.

Natural convection in an enclosure under the Boussinesq approximation has been studied numerically for a wide range of Rayleigh numbers. 12-14 Beyond the critical Rayleigh number, the flow transitions from the steady regime to unsteady flow regime, and the centrosymmetric flow structure is broken. Vortices are generated in the detached region near the cavity corners and along the isothermal walls. The unsteady convection is affected by several controlling parameters. Janssen and Henkes⁶ found that for Prandtl number between 0.25 and 2.0, the flow transition experiences periodic and quasi-periodic motion before reaching a turbulent flow. However, for Prandtl number between 2.5 and 7.0, there is no intermediate flow regime, and the flow goes from steady to turbulent. Paolucci and Chenoweth⁷ proposed that for cavity with aspect ratio $\frac{1}{2} \le A \le 3$ (A = H/L, H is cavity height, L is cavity length), the instability first takes place near the departing corners; for a shorter or taller cavity, the primary instability happens inside the boundary layer along the isothermal wall. Using the pseudo-spectral method, Quéré and Behnia⁸ claimed that the critical Rayleigh number of transition to unsteadiness is $Ra_{cr} = 1.82$ $\pm 0.01 \times 10^8$ for an air-filled square cavity under the Boussinesq approximation. With respect to the instability mechanism for an airfilled square cavity, researchers reached an agreement that there are two types of instability mechanisms.^{6,7} The primary instability happens in the detached region near the horizontal walls.^{8,15} This sheardriven, Kelvin-Helmholtz type instability occurs in a jet-like fluid layer where the vertical boundary layers are turned horizontal. When the Rayleigh number is further increased, the second instability (boundary layer instability) takes place inside the vertical boundary layer along the isothermal wall. Although the central-symmetry is broken at high Rayleigh number, two types of instability mentioned above are observed for both the hot wall and cold wall region.

As the turbulent convection is essentially three-dimensional in nature, researchers extend direct numerical simulation (DNS) to three-dimensional enclosures. ^{15–17} Labrosse *et al.* ¹⁸ claimed that the transition to unsteadiness happens at $Ra = 3.19 \times 10^7$ using the pseudo-spectral method. Trias *et al.* ¹⁹ provided a comparison between two- and three-dimensional numerical results. They claimed the flow experiences laminar, periodic, and quasi-periodic and eventually become turbulent in the vertical boundary layer along the isothermal

Comparing to Boussinesq-type natural convection, compressible natural convection is more complex due to the fluid density variation and local compressibility. Most previous studies of compressible natural convection are performed under low Mach number approximation²⁰ or using steady Navier–Stokes equations.^{21,22} The laminar flow regime of compressible natural convection is studied by researchers using different numerical methods.^{23–26} Chenoweth and Paolucci provided early steady-state two-dimensional results using the finite-difference method under the low Mach number approximation.²⁷ The governing equation is an approximation of the compressible

Navier-Stokes equation; the total pressure is decomposed and only thermodynamic pressure is considered in the equation of state. Using the steady two-dimensional Navier-Stokes equations, Vierendeels et al.²¹ performed a set of numerical simulations up to Rayleigh number $Ra = Pr2\varepsilon g L^3 \rho_0^2 / \mu_0^2 = 1.0 \times 10^7$, where $\varepsilon = (T_h - T_c)/(2T_0)$, ρ_0 , μ_0 are density and viscosity at the average temperature $T_0 \equiv (T_h + T_c)/2$. There are only very few results available for unsteady compressible natural convection. Quéré et al.²⁸ investigated the transition to unsteady non-Boussinesq natural convection in a tall cavity using a pseudo-spectral algorithm. They showed that the temperature difference parameter ε has a significant effect on the critical Rayleigh number. The flow is more unstable with a large value of ε . Recently, Lenz et al.²⁹ reported a GKS (gas-kinetic scheme) result of unsteady natural convection with Rayleigh number $Ra = 5.0 \times 10^9$. They showed that the flow field is highly asymmetric and proposed that the heating decreases the boundary layer stability and cooling increases the boundary layer stability. Wen et al.³⁰ performed twoand three-dimensional simulation of compressible natural convection with Rayleigh number up to $Ra = 5.0 \times 10^9$ using the discrete unified gas-kinetic scheme (DUGKS). Table I provides a summary of studies on compressible natural convection flows, comparing numerical methods and the setting of the flow and the range of Rayleigh numbers. In general, the transition to the unsteady compressible natural convection in an enclosure is still largely unexplored.

The instability mechanism of the compressible natural convection is expected to be different from the Boussinesq convection. As the compressible natural convection in an enclosure is not symmetric in the steady regime, namely, the fluid is thermodynamically expanded near the hot wall and contracted near the cold wall, this density variation of the fluid introduces another unstable mechanism to the flow evolution. To investigate the onset of unsteady compressible natural convection, fully compressible Navier-Stokes equations are required for the simulation. The fully compressible Navier-Stokes equations can be properly recovered by a modeled Boltzmann equation. Among these kinetic models, the coupled double-distribution function (DDF) model is widely used in thermal flow simulations due to its inner coherence in physics and simplicity in implementation.³⁰ The viscous dissipation and the compression work are considered in these coupled thermal DDF models. Two reduced distributions are derived from the original higher-dimensional particle distribution by integrating out the internal degrees of freedom. The density and velocity fields are determined by the first reduced distribution function. The choice for the second reduced distribution function can be flexible, whose integral may be related to the internal energy, 37,42 total 9,43 or partial internal energy. 30,44 It is worth pointing out that not all of the above works are capable of simulating the compressible natural convection with a large temperature. For a successful simulation of compressible natural convection, the Hermite expansion of equilibrium distribution to an adequate order is required. ⁴⁵ The DDF model can be a desired choice for compressible natural convection simulation because we only need to solve a quasi-linear equation. In this study, we perform a set of numerical simulations at different Rayleigh numbers, beyond the critical Rayleigh number to inquire into the instability mechanism, using the discrete unified gas-kinetic scheme (DUGKS). As a newly developed method, 44,46 DUGKS has been applied to nearly incompressible thermal flow 12,47,48 and compressible flow, 30,41,49,50 and proved to be an accurate and robust

TABLE I. Studies of compressible natural convection.

	Method	Dimension and resolution	A	Ra
Chenoweth and Paolucci ²⁷	Finite difference (FD)	2D (121 × 121)	1–10	$10^3 - 10^7$
Quéré et al. 28,31,32	Spectral	$2D (80 \times 80, 32 \times 96)$	1, 8	$10^5, 10^6$
Vierendeels et al. ^{21,22}	FV	$2D (512 \times 512)$	1	$10^2 - 10^7$
Becker and Braack ²³	Finite element (FE)	2D [4×10^6 degrees of freedom (DOF)]	1	$10^6 - 10^7$
Li et al. ²⁶	LBM	$2D(250 \times 250)$	1	$10^3 - 10^5$
Feng <i>et al.</i> ^{33,34}	LBM	$2D (100 \times 100 \times 10)$	1	$10^3 - 10^5$
Lenz et al. ²⁹	GKS	$2D(376 \times 376)$	1	$10^6, 5 \times 10^9$
Wang et al. ³⁵	FD	$2D(512 \times 512)$	1	$10^5 \sim 10^9$
Wen et al. ³⁰	DUGKS	$2D(360 \times 360)$	1	$10^6, 5 \times 10^9$

method. Due to the finite-volume formulation, non-uniform meshes can be easily implemented by DUGKS. The numerical instability can be largely improved by the use of nonuniform mesh. ^{51,52} The boundary condition is applied right at the cell interfaces which coincide with the wall. Besides, for continuum flows, DUGKS can be viewed as a special finite-volume lattice Boltzmann method (FV-LBM), but it is more accurate and robust than FV-LBM. ⁵³

There are several important issues to be addressed when investigating the transition to unsteady compressible natural convection in an enclosure using DUGKS. The first one is to recover the fully compressible Navier–Stokes equations. We choose the Boltzmann equation with the simple Bhatnagar–Gross–Krook (BGK) collision model, 44,54 instead of the BGK-Shakhov model or ellipsoidal-statistical model. An extra source term is introduced to adjust the Prandtl number. The second issue is the proper implementation of the temperature and velocity boundary condition. The velocity and the temperature field are strongly coupled in compressible thermal flows. The boundary condition used in this study is properly derived by the Chapman–Enskog analysis, so the consistency with the Navier–Stokes–Fourier equations is ensured at the wall. The details of source term design and the boundary condition derivation can be found in our other paper. The stokes of the surface of

The primary goal of this paper is to investigate the development of non-Boussinesq unsteady natural convection in a square cavity using DUGKS. A detailed analysis of the unsteady flow structure and the instability mechanism is presented and compared to the Boussinesq-type convection. This paper is organized as follows. In Sec. II, we describe the physical problem and the governing equations. In Sec. III A, we determined the critical Rayleigh number for the transition from steady to unsteady flow. Numerical results at three moderate Rayleigh numbers $1.83 \times 10^8, 3.0 \times 10^8$, and 5.0×10^8 are presented and analyzed in Sec. III B. The natural convection with a high Rayleigh number $Ra = 5.0 \times 10^9$ is shown in Sec. III C. The main contributions and conclusions of this work are summarized in Sec. IV.

II. PROBLEM DESCRIPTION AND NUMERICAL METHOD

A. Problem description

The physical configuration under consideration here is an air-filled (Pr = 0.71) square cavity with adiabatic top and bottom walls, the left wall is heated (with temperature held at T_h), and the right wall is cooled (with temperature held at T_c), as shown in Fig. 1.

Alternatively, T_h and T_c can be replaced by the average temperature $T_0 \equiv (T_h + T_c)/2$ and dimensionless temperature difference $\varepsilon \equiv (T_h - T_c)/(2T_0)$, namely, $T_h = T_0(1+\varepsilon)$ and $T_c = T_0(1-\varepsilon)$. The no-slip boundary condition $\boldsymbol{u}_w = 0$ is applied for all walls. When $\varepsilon \ll 1$, the convection can be studied under the Boussinesq assumption; otherwise, the flow is governed by the compressible Navier–Stokes–Fourier equations, which can be written as

$$\frac{\partial \rho}{\partial t} + \frac{\partial (\rho u_j)}{\partial x_i} = 0, \tag{1a}$$

$$\frac{\partial(\rho u_i)}{\partial t} + \frac{\partial(\rho u_i u_j)}{\partial x_j} = -\frac{\partial p}{\partial x_i} + \rho g_i + \frac{\partial \sigma_{ij}}{\partial x_j},\tag{1b}$$

$$\frac{\partial(\rho C_V T)}{\partial t} + \frac{\partial(\rho u_j C_V T)}{\partial x_j} = -p \frac{\partial u_j}{\partial x_j} + \frac{\partial}{\partial x_j} \left(k \frac{\partial T}{\partial x_j}\right) + \sigma_{ij} \frac{\partial u_j}{\partial x_j}, \quad (1c)$$

$$p = \rho RT, \tag{1d}$$

where the stress tensor is $\sigma_{ij} = 2\mu \left(S_{ij} - \frac{1}{D}\nabla \cdot \boldsymbol{u}\delta_{ij}\right) + \mu^{V}\nabla \cdot \boldsymbol{u}\delta_{ij}$, S_{ij} is the strain rate tensor, and μ and μ^{V} are the shear viscosity and the bulk viscosity, respectively. The fluid properties are temperature dependent in the compressible case; the viscosity and heat conductivity are given by Sutherland's law,

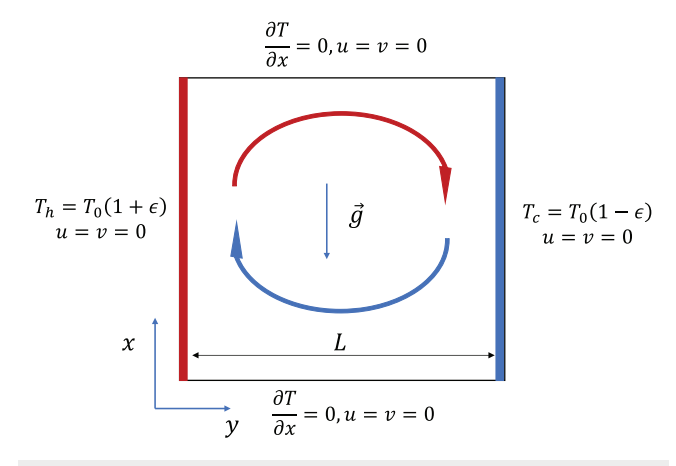


FIG. 1. The geometry under consideration.

$$\frac{\mu(T)}{\mu^*} = \left(\frac{T}{T^*}\right)^{3/2} \frac{T^* + S}{T + S}, \quad k(T) = \frac{\mu(T)C_p}{Pr}, \tag{2}$$

where $T^*=273\,\mathrm{K}$ and $S=110.5\,\mathrm{K}$. The parameter μ^* is calculated by $\mu^*=\mu_0[\left(\frac{T_0}{T^*}\right)^{3/2}\frac{T^*+S}{T_0+S}]^{-1}$, where μ_0 is the viscosity at a reference temperature $\mu_0(Ra)=\mu(T_0)$. The governing equations can be normalized by the following reference quantities: a reference density scale ρ_0 , a reference length scale L, a reference velocity scale $u_0=\sqrt{(T_h-T_c)gL/T_0}$, a reference time scale L/u_0 , a reference temperature scale $T_0=(T_h+T_c)/2$, a reference viscosity $\mu_0=\mu(T_0)$, and a reference conductivity $k_0=k(T_0)$. With these reference scales, the dimensionless compressible Navier–Stokes–Fourier equations can be written as

$$\frac{\partial \hat{\rho}}{\partial \hat{t}} + \frac{\partial \left(\rho \hat{u}_{j}\right)}{\partial \hat{x}_{i}} = 0, \tag{3a}$$

$$\frac{\partial (\hat{\rho}\hat{u}_i)}{\partial \hat{t}} + \frac{\partial (\hat{\rho}\hat{u}_i\hat{u}_j)}{\partial \hat{x}_j} = -\frac{\partial \hat{p}}{\partial \hat{x}_i} + \frac{1}{2\varepsilon}\hat{\rho}\delta_{i1} + \sqrt{\frac{Pr}{Ra}}\frac{\partial \hat{\sigma}_{ij}}{\partial \hat{x}_j}, \quad (3b)$$

$$\begin{split} \frac{\partial \left(\hat{\rho}\,\hat{T}\right)}{\partial \hat{t}} + \frac{\partial \left(\hat{\rho}\,\hat{u}_{j}\,\hat{T}\right)}{\partial \hat{x}_{j}} &= \Lambda \left[-\hat{p}\,\frac{\partial \hat{u}_{j}}{\partial \hat{x}_{j}} + \frac{\gamma}{\Lambda\sqrt{RaPr}}\frac{\partial}{\partial \hat{x}_{j}}\left(\hat{k}\,\frac{\partial \hat{T}}{\partial \hat{x}_{j}}\right) \right. \\ &\left. + \sqrt{\frac{Pr}{Ra}}\hat{\sigma}_{ij}\frac{\partial \hat{u}_{j}}{\partial \hat{x}_{j}}\right], \end{split} \tag{3c}$$

where $\Lambda \equiv \gamma(\gamma-1)Ma^2$. The dimensionless parameters in the governing equations are the dimensionless temperature difference ε , Rayleigh number $Ra = \frac{Pr2\varepsilon_0 L^3 \rho_0^2}{\mu_0^2}$, Prandtl number $Pr \equiv \mu_0 C_p/k(T_0)$ (fixed at 0.71 here for air), Mach number $Ma = u_0/c_s(T_0) = \sqrt{\frac{2\varepsilon_0 L}{\gamma R T_0}}$, and heat capacity ratio $\gamma = C_p/C_V = 1.4$. In our study, fully compressible Navier–Stokes equations are employed for time-dependent compressible thermal flow, and no Boussinesq approximation or low Mach number approximation is made. By choosing different temperature differences, both the Boussinesq flow and compressible natural convection flow can be studied.

B. The numerical method

In this study, a mesoscopic computational method based on a model Boltzmann equation is used to simulate the natural convection flow. To recover the fully compressible Navier–Stokes equations, we employ the Boltzmann equation with the Bhatnagar–Gross–Krook (BGK) model used by Guo *et al.*⁴⁴ An extra source term S_f is introduced to the kinetic model, which is capable of incorporating an arbitrary Prandtl number. The derivation details are shown in our other paper;³⁰ we do not repeat here for the sake of simplicity,

$$\frac{\partial f}{\partial t} + \boldsymbol{\xi} \cdot \nabla_{\mathbf{x}} f + \boldsymbol{b} \cdot \nabla_{\boldsymbol{\xi}} f = -\frac{f - f^{eq}}{\tau} + S_f, \tag{4}$$

where $f(\mathbf{x}, \boldsymbol{\xi}, \boldsymbol{\eta}, \boldsymbol{\zeta}, t)$ is the distribution function describing the motion of particles at the location $\mathbf{x} = (x_1, ..., x_D)$ and time t with microscopic velocity $\boldsymbol{\xi} = (\xi_1, ..., \xi_D)$, where D is the spatial dimension of the hydrodynamic velocity \boldsymbol{u} . The remaining (3D) space of the microscopic velocity is denoted by $\boldsymbol{\eta}$. Furthermore, an internal kinetic variable, $\boldsymbol{\zeta}$, of dimension K is introduced in order to adjust the specific

heat ratio of the model. The external force per unit mass is given by b, and τ is the relaxation time. The Maxwellian equilibrium is given as

$$f^{eq} = \frac{\rho}{(2\pi RT)^{(3+K)/2}} \exp\left(-\frac{c^2 + \eta^2 + \zeta^2}{2RT}\right),\tag{5}$$

where $c \equiv \xi - u$ is the peculiar velocity. The hydrodynamic (conservative) flow variables can be obtained by the moments of the distribution function.

$$\rho = \int f d\xi d\eta d\zeta, \quad \rho \mathbf{u} = \int \xi f d\xi d\eta d\zeta, \quad \rho E = \int \frac{\xi^2 + \eta^2 + \zeta^2}{2} f d\xi d\eta d\zeta,$$
(6)

and the Maxwellian equilibrium implies that $\rho E = \rho u^2/2 + \rho c_V T$ with $c_V = (3+K)R/2$ being the specific heat capacity at constant volume. The specific heat ratio for the model is $\gamma = (5+K)/(3+K)$, yielding the specific heat ratio of the air $\gamma = 1.4$ when K = 2. From the Chapman–Enskog analysis, the fluid properties of the model can be derived, and they are

$$\mu = p\tau, \ \mu^{V} = \left(\frac{2}{D} - \frac{2}{K+3}\right)p\tau, \ k = \frac{\mu C_{p}}{Pr} = \frac{p\tau}{Pr}\frac{(K+5)R}{2}.$$
 (7)

In order to incorporate an arbitrary Prandtl number, we introduce an extra source term S_f to the kinetic model. The source term is designed as

$$S_f = \tilde{\omega} \left[\frac{\eta^2 + \zeta^2}{(K + 3 - D)RT_0} - 1 \right] \frac{(1 - Pr)q_i \xi_i}{\tau(\sqrt{RT_0})^{4 - D}}, \tag{8}$$

where $\tilde{\omega}(\xi, \eta, \zeta) = \frac{1}{(\sqrt{2\pi R T_0})^{K+3}} \exp\left(-\frac{\xi^2 + \eta^2 + \xi^2}{2R T_0}\right)$ is the weighting function, and q_i is the heat flux which can be calculated from the distribution function by

$$q_i = \frac{1}{2} \int c_i(c^2 + \eta^2 + \zeta^2) f d\xi d\eta d\zeta. \tag{9}$$

For efficient numerical implementation, it is more convenient to first integrate out the inactive degree of freedoms (η, ζ) by introducing two reduced distributions $g(x, \xi, t)$ and $h(x, \xi, t)$,

$$g(\mathbf{x}, \xi, t) = \int f(\mathbf{x}, \xi, \eta, \zeta, t) d\eta d\zeta, \tag{10a}$$

$$h(\mathbf{x}, \boldsymbol{\xi}, t) = \int (\eta^2 + \zeta^2) f(\mathbf{x}, \boldsymbol{\xi}, \boldsymbol{\eta}, \zeta, t) d\boldsymbol{\eta} d\zeta.$$
 (10b)

Correspondingly, the governing equation for $g(x, \xi, t)$ and $h(x, \xi, t)$ can be obtained as

$$\frac{\partial g}{\partial t} + \xi \cdot \nabla_{x} g + \boldsymbol{b} \cdot \nabla_{\xi} g = \Omega_{g} = -\frac{g - g^{eq}}{\tau}, \tag{11a}$$

$$\frac{\partial h}{\partial t} + \boldsymbol{\xi} \cdot \nabla_{\boldsymbol{x}} h + \boldsymbol{b} \cdot \nabla_{\boldsymbol{\xi}} h = \Omega_h = -\frac{h - h^{eq}}{\tau} + S_h, \tag{11b}$$

$$S_h = \frac{\omega(\xi)}{\tau} \left\{ \frac{2(1 - Pr)q_i}{\sqrt{RT_0}} \frac{\xi_i}{\sqrt{RT_0}} \right\},\tag{11c}$$

where $\omega(\xi) = \frac{1}{(\sqrt{2\pi R T_0})^D} \exp\left(-\frac{\xi^2}{2R T_0}\right)$. In this double distribution function model, density and velocity are determined by $g(x, \xi, t)$ and energy is determined by $g(x, \xi, t)$ and $h(x, \xi, t)$ together,

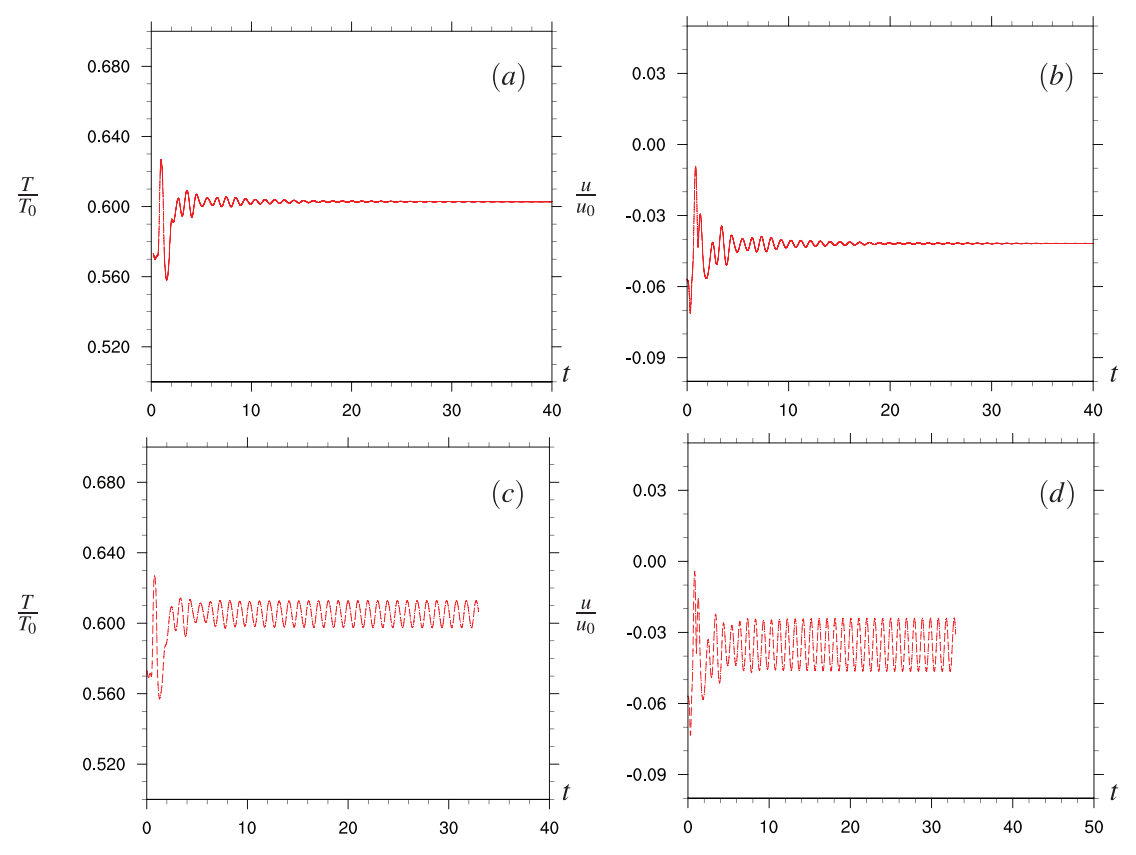


FIG. 2. Time trace of temperature $\frac{T(t)}{T_0}$ and velocity $\frac{u(t)}{u_0}$ at location (x,y)=(0.1,0.82)L for: (a) and (b) $Ra=4.05\times10^7,\ \epsilon=0.6$ and (c) and (d) $Ra=4.25\times10^7,\ \epsilon=0.6$.

$$\rho = \int g d\xi, \quad \rho \mathbf{u} = \int \xi g d\xi, \quad \rho E = \frac{1}{2} \int (\xi^2 g + h) d\xi. \tag{12}$$

The Maxwellian equilibrium g^{eq} and h^{eq} take the following forms:

$$g^{eq} = \int f^{eq} d\boldsymbol{\eta} d\zeta = \frac{\rho}{(2\pi RT)^{D/2}} \exp\left[-\frac{(\boldsymbol{\xi} - \boldsymbol{u})^2}{2RT}\right], \quad (13a)$$

$$h^{eq} = \int (\eta^2 + \zeta^2) f^{eq} d\eta d\zeta = (K + 3 - D) R T g^{eq}.$$
 (13b)

For a continuum flow, the forcing term F_{ϕ} can be approximated by

$$F_{\phi} = -\boldsymbol{b} \cdot \nabla_{\xi} \phi \approx -\boldsymbol{b} \cdot \nabla_{\xi} \phi^{eq} = \frac{\boldsymbol{b} \cdot (\xi - \boldsymbol{u})}{RT} \phi^{eq}, \quad (14)$$

TABLE II. Parameters for the simulation of natural convection with a large temperature difference.

Ra	Pr	γ	3	Ма
$1.83 \sim 5.0 \times 10^8$	0.71	1.4	0.6	0.1
$p_0 (\mathrm{kg/ms^2})$	$T_0(K)$	$R \left(\mathrm{m}^2/\mathrm{s}^2 \mathrm{K} \right)$	$g\left(\frac{m}{s^2}\right)$	μ_0
101 325.0	600.0	287	g(Ma)	$\mu_0(Ra)$

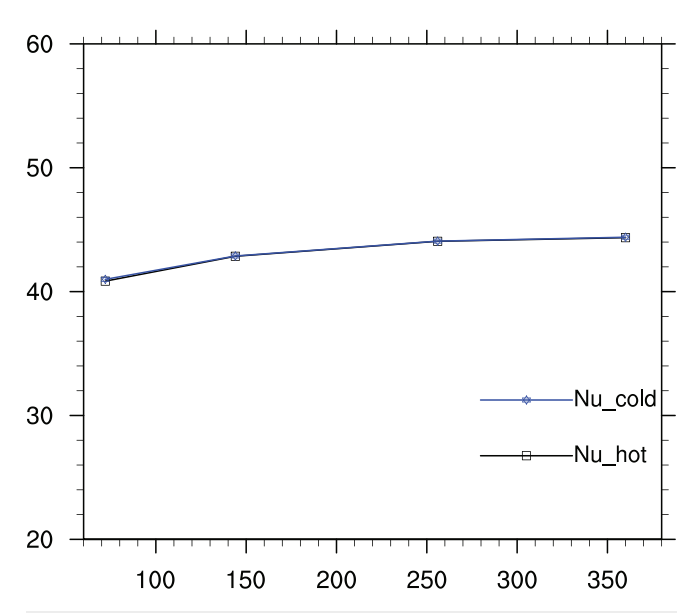


FIG. 3. The convergence study of overall Nusselt number with $Ra=5.0\times10^8$ and $\varepsilon=0.6$.

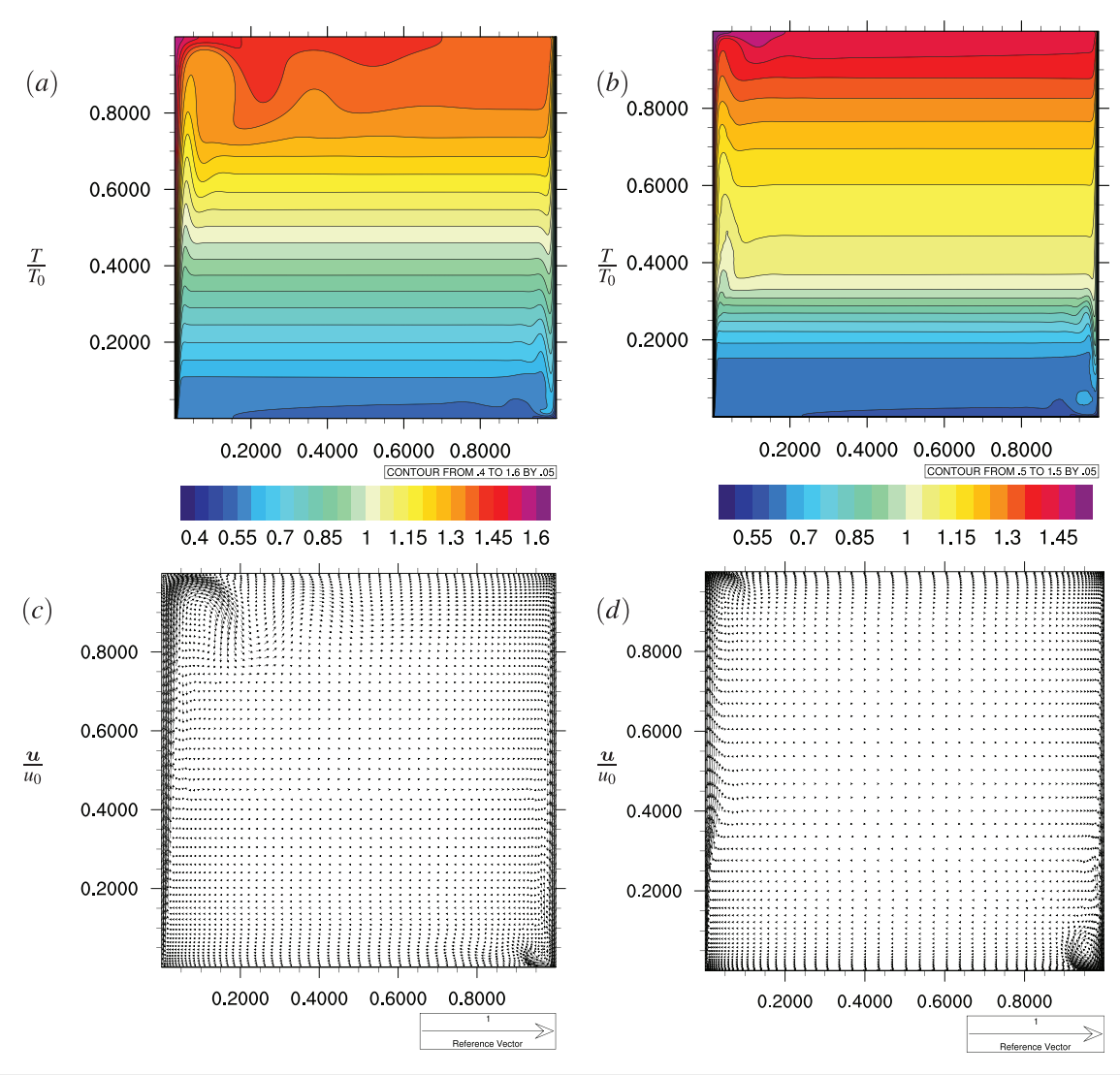


FIG. 4. Time-averaged isotherms and velocity vector plot for (a) and (c) $Ra = 5.0 \times 10^8$, $\epsilon = 0.6$ and (b) and (d) $Ra = 5.0 \times 10^9$, $\epsilon = 0.6$.

TABLE III. Characteristic values, $Ra=10^8\sim 10^9$. u_{max} (u_{min}) is the maximum (minimum) value of the time-averaged vertical velocity of the whole cavity; $u_{max,mid}$ ($u_{min,mid}$) is the maximum (minimum) value of the time-averaged vertical velocity at the mid-height, and $\delta_{u_{max,mid}}$ ($\delta_{u_{min,mid}}$) denotes the distance between the isothermal wall and the horizontal location of the maximum (minimum) velocity $u_{max,mid}$ ($u_{min,mid}$); $\delta_{hot,mid}$ ($\delta_{cold,mid}$) represents the velocity boundary layer thickness at the mid-height (the distance between the isothermal wall and the location of $u=0.1\%u_{max}$).

Ra	1.83×10^{8}	3.0×10^{8}	5.0×10^{8}	1.5×10^{9}	3.0×10^{9}	5.0×10^{9}
$u_{\rm max}/u_0$	0.2844	0.2837	0.2825	0.2823	0.2780	0.2618
$u_{\max,mid}/u_0$	0.2701	0.2690	0.2675	0.2674	0.2429	0.1173
$\delta_{u_{ ext{max},mid}}/L$	1.5221×10^{-2}	1.3748×10^{-2}	1.2306×10^{-2}	8.4952×10^{-3}	8.4952×10^{-3}	7.4802×10^{-3}
u_{\min}/u_0	-0.2540	-0.2535	-0.2534	-0.2528	-0.2640	-0.2903
$u_{\min,mid}/u_0$	-0.2515	-0.2509	-0.2514	-0.2509	-0.2638	-0.2595
c /-	6.8260×10^{-3}	6.8260×10^{-3}	5.5260×10^{-3}	4.7710×10^{-3}	3.8750×10^{-3}	2.8410×10^{-3}
$rac{\delta_{u_{\min,mid}}/L}{\delta_{hot,mid}}$	1.1503	1.1055	1.1259	1.1488	1.1100	2.1516

where ϕ represents g or h. The Prandtl number correction term S_h in Eq. (11c) only contributes to the first order momentum of h, which is the component of heat flux $q_i = \frac{1}{2} \int c_i(c^2g + h)d\xi$. In this way, we overcome the unity Prandtl number limitation of the original BGK model without changing the continuity and momentum equations, and it is worth pointing out that the current model only requires up to the fourth order Hermite expansion of the equilibrium and the Gauss quadrature with an eighth degree of precision. In our current study, the D2Q25 model with a ninth degree of quadrature precision is used.

For our physical problem, we have no-slip condition (u = 0) for all walls. The vertical walls are at a fixed temperature, while the top and bottom walls are insulated ($\frac{\partial T}{\partial x} = 0$). Appropriate boundary treatment should be applied for the distribution functions. We

develop a systematic approach to derive the boundary conditions for temperature and velocity based on the Chapman–Enskog analysis and Hermite expansion of equilibrium. The bounce-back boundary expressions are shown in A. DUGKS developed by Guo et al. References 44 and 46 are used for the current work. As a finite-volume method, the nonuniform mesh can be easily implemented by DUGKS, which is desired for resolving the sharp temperature and velocity gradient near the walls. The implementation of DUGKS is the same as the work of Guo et al. 46 and Wang et al. 12 The time step is determined by the Courant–Friedrichs–Lewy (CFL) condition $\Delta t = CFL \frac{\Delta x_{\min}}{U_{\max} + \xi_{\max}}$ (U_{\max} is the maximum flow velocity, and ξ_{\max} is the maximum discrete velocity). 44 The CFL number for all simulations is set to be 0.5. To resolve the steep

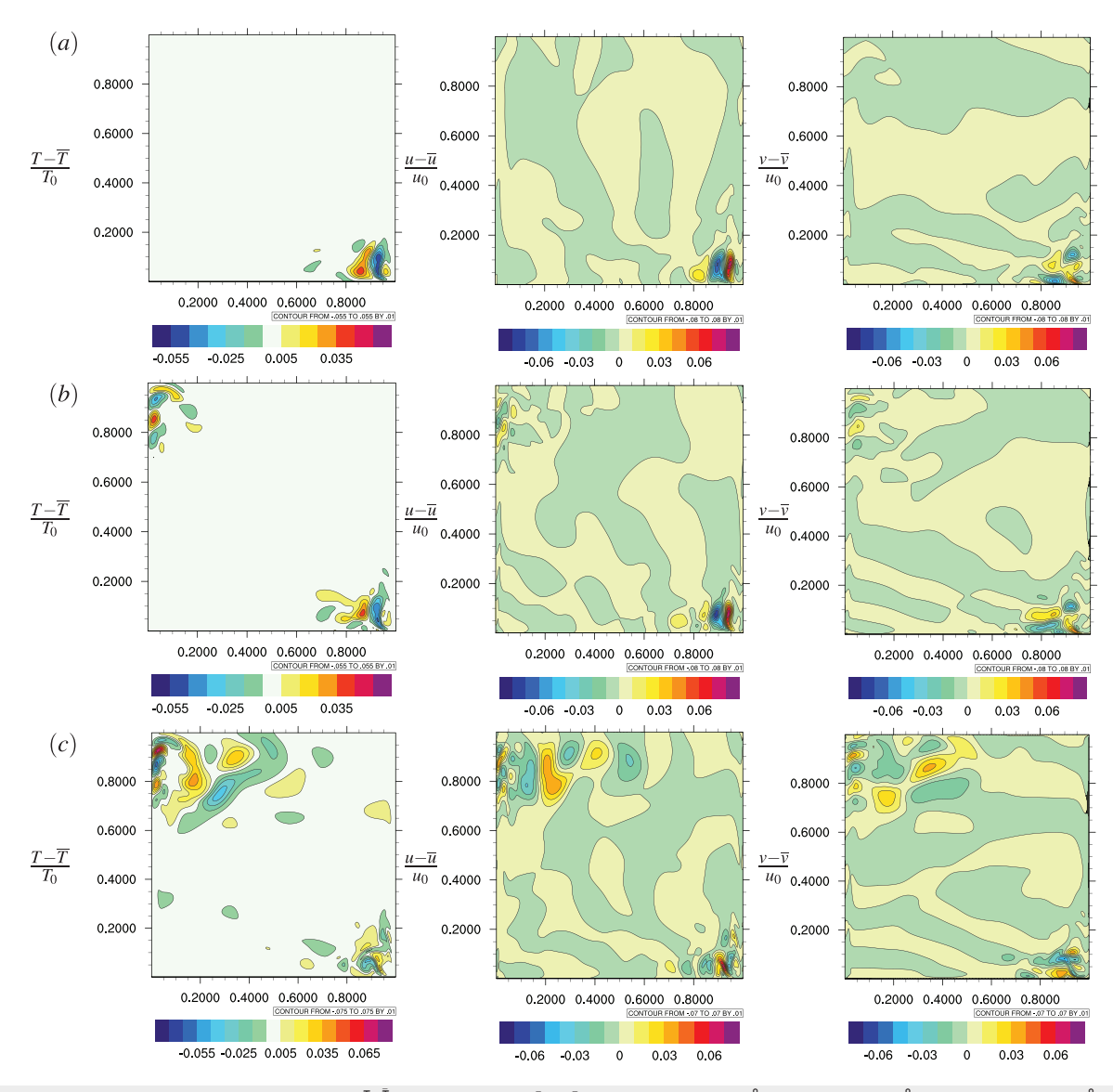


FIG. 5. Instantaneous fluctuation temperature $\frac{T-\bar{T}}{T_0}$ and velocity field $\frac{u-\bar{u}}{u_0}$, $\frac{v-\bar{v}}{u_0}$ for (a) $Ra=1.83\times10^8$, (b) $Ra=3.0\times10^8$, and (c) $Ra=5.0\times10^8$

gradients of velocity and temperature near the wall, nonuniform meshes are employed in each direction. For a set of stretched meshes with N grid points in each direction, the location of the cell interface $x_b(i)$ is given by

$$x_b(i) = \frac{1}{2} \left[1 + \frac{\tanh[S(i/N - 0.5)]}{\tanh(S/2)} \right], \quad i = 0, 1, 2, ..., N,$$
 (15)

where *S* is the parameter used to adjust the degree of nonuniformity. Then the location of the cell center can be obtained by $x(i) = [x_b(i) + x_b(i+1)]/2$. The code was run on the National Center for Atmospheric Research's (NCAR-Wyoming) Supercomputer, known as Cheyenne, equipped with 2.3-GHz Intel Xeon E5–2697V4 processors. The computational domain are decomposed in the *y*, and 128 processors are employed for the case with mesh N=256. The wall clock time per step is 1.86×10^{-3} s.

III. RESULTS AND DISCUSSION

A. The critical Rayleigh number

Figure 2 presents the time trace of temperature $T(t)/T_0$ and vertical velocity $u(t)/u_0$ at the monitoring point for $Ra = 4.05 \times 10^7$ and $Ra = 4.25 \times 10^7$. The time integration for both cases was started from the steady solution at $Ra = 3.0 \times 10^7$. A fine mesh 500×500

under a given nonuniform grid setting, as described below in Sec. II B, with $\Delta x_{min} = 6.022 \times 10^{-4} \, \text{L}$ is used to evaluate the critical Rayleigh number to make sure that the critical Rayleigh number is properly converged; at lower grid resolutions, it was found that the critical Rayleigh number could be under-estimated. The location of the monitoring point is chosen based on the instantaneous fluctuation contours of temperature and velocity, where the primary instability first occurs. For the case $Ra = 4.05 \times 10^7$, the solution first experiences damped oscillations and then reaches a steady state. For the case Ra = 4.25 $\times 10^7$, the periodic oscillation result is obtained, which indicates the flow becomes unsteady. Therefore, we can claim that $Ra_{cr}=(4.15\pm0.10)$ $\times 10^7$, which is significantly lower than $Ra_{cr} = (1.82 \pm 0.01) \times 10^8$ for natural convection at small ε . Wang et al. 35 solved the low-Mach-number equations (Paolucci²⁰) and provided results up to $Ra = 10^9$. The critical Rayleigh number they predicted was $Ra_{cr}=2.35\pm0.05\times10^7$, and it is slightly lower than what we obtained here using the fully compressible Navier-Stokes equations. In Sec. III B, we will continue to investigate the development of unsteady flow and instability mechanism.

B. The development of unsteady convection

To investigate the transition from steady to unsteady compressible natural convection in the square cavity with a large temperature

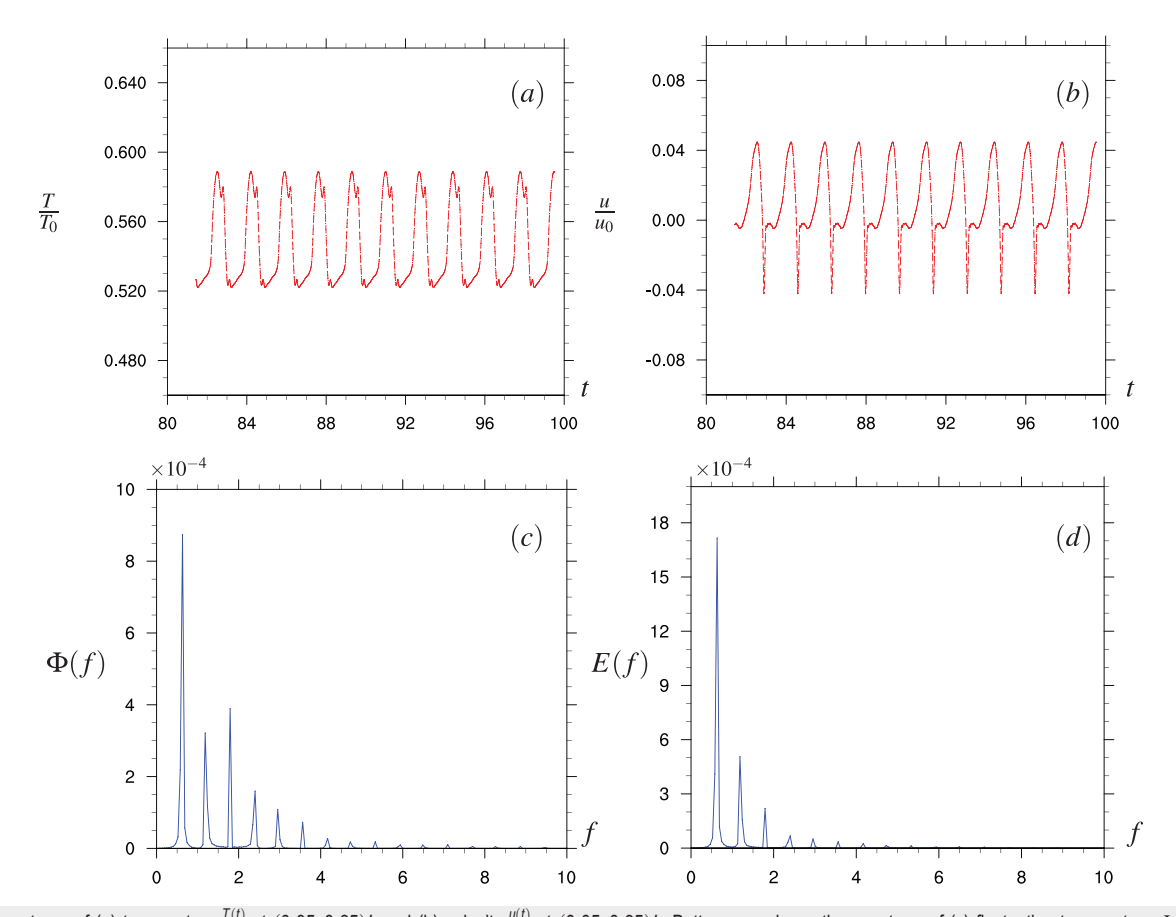


FIG. 6. Time trace of (a) temperature $\frac{T(t)}{T_0}$ at (0.05, 0.85)L and (b) velocity $\frac{u(t)}{u_0}$ at (0.05, 0.95)L. Bottom row shows the spectrum of (c) fluctuation temperature $\Phi(f)$ and (d) vertical velocity E(f). $Ra = 1.83 \times 10^8$.

difference $\varepsilon = 0.6$, we perform a set of simulations with Rayleigh numbers beyond the critical value. As pointed out by Quéré et al.,2 with a large temperature difference, the flow is more unstable than the Boussinesq convection. Three simulations with Rayleigh number 1.83×10^{8} , 3.0×10^{8} , 5.0×10^{8} are performed to explore the transition from steady to unsteady in compressible natural convection. Table II shows the parameter setting for these simulations. Figure 3 shows the convergence study of the overall Nusslet number at Ra $=5.0\times10^8$ with different meshes. The relative difference between last two meshes 256×256 and 360×360 is less than 1%. Accurate results can be obtained with a nonuniform resolution of 256 × 256 $(S = 3, \Delta x_{\min} = 1.182 \times 10^{-3} \text{ L})$. The simulations in Sec. III B are performed with the nonuniform mesh 256 × 256 unless otherwise stated. In our mesoscopic method, Nusselt number can be obtained directly through the distribution function, most conveniently at the cell interface at the half time steps in DUGKS, as

$$Nu(x) = \frac{L}{k_0(T_h - T_c)} k \frac{\partial T}{\partial y} \bigg|_{wall} = -\frac{L}{k_0(T_h - T_c)} q_y, \quad (16)$$

where q_y can be computed using the distribution function as $q_y = \frac{1}{2} \int c_y (c^2g + h) d\xi$.

Figure 4 shows time-averaged temperature field and velocity vector plot of cases $Ra = 5.0 \times 10^8$ and $Ra = 5.0 \times 10^9$ when the flow becomes statistically stationary. The averaging was performed over a duration of $30 \times [4L/(u_0/3)]$ for the former case and $75 \times [4L/(u_0/3)]$ for the latter case. Driven by buoyancy force, the hot fluid arises along with the hot wall, and the cold fluid descends along the cold wall and forms a recirculation in the cavity. Unlike Boussinesq-type convection, compressible natural convection is featured by heating expansion near the hot wall and cooling compression near the cold wall. Table III tabulates some characteristic values of the simulated flows at different Rayleigh numbers when the flow reaches the statistically stationary stage. For cases $Ra = 1.83 \sim 5.0 \times 10^8$, the maximum value of the time-averaged vertical velocity near the hot wall, $|u_{\text{max}}|$, is larger than the minimum value of the time-averaged vertical velocity near the cold wall, $|u_{\min}|$. The boundary layer thickness of the cold wall $\delta_{u_{\min,mid}}$ is significantly smaller than that for the hot wall $\delta_{u_{\max,mid}}$. These characteristic values further indicate that the flow is highly asymmetric for natural convection with a large temperature difference. These flow features are distinct from the Boussinesq cases. In Secs. III B and III C, we will show the asymmetry of the flow instability for the hot wall region and the cold wall region.

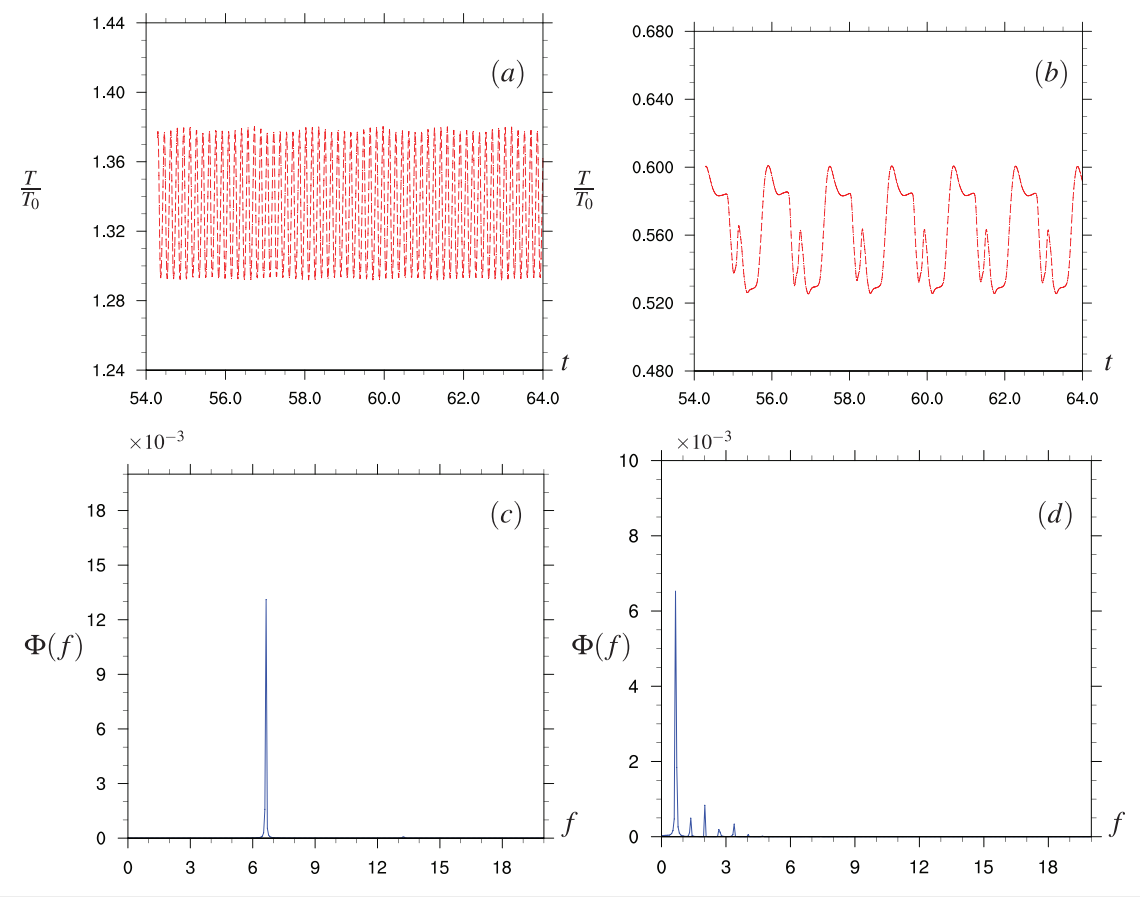


FIG. 7. Top: time trace of temperature $\frac{T(f)}{T_0}$ (top) and their spectrum of temperature $\Phi(f)$ (bottom) at monitoring points with $Ra = 3.0 \times 10^8$, (a) and (c) for point (0.85, 0.025)L, (b) and (d) for point (0.07, 0.85)L.

To illustrate the flow structure, the instantaneous fluctuation temperature $(T-\bar{T})/T_0$ and velocity components $(u-\bar{u})/u_0$, $(v-\bar{v})/u_0$ at three Rayleigh numbers are displayed in Fig. 5. Time-averaged fields are computed when the flow reaches stationary state; these instantaneous contours are informative and clearly elucidate the unstable flow structures. From Fig. 5(a), we can observe that the temperature and velocity fluctuations concentrate at the right bottom corner near the bottom adiabatic wall for $Ra=1.83\times 10^8$. There are two large vortex structures in the fluctuation contours. The instability first appears near the bottom corner of cold wall. The data in Table III suggest that the magnitude of velocity gradient on the cold wall is larger than that on the hot wall due to the difference in the boundary thicknesses on the two walls. This could be the reason for stronger vortices at the right bottom corner.

Based on these instantaneous fluctuation contours, monitoring points are chosen near the center of the fluctuation fields. Figures 6(a) and 6(b) show the time trace of temperature and velocity at monitoring points which clearly demonstrate the time-periodic behaviors. The non-dimensional time t is defined as $t=\frac{(u_0/3)\tilde{t}}{4L}$ and frequency is normalized by $\frac{4L}{(u_0/3)}$, $u_0/3$ is approximately the maximum velocity and 4L is the perimeter of the cavity enclosure. The spectrum of fluctuation temperature $\Phi(f_i)$ and velocity $E(f_i)$ are given in Figs. 6(c) and 6(d), where

$$\frac{1}{2}\langle \hat{u}'^2 \rangle = \sum_{i} E(f_i),$$

$$\langle \hat{T}'^2 \rangle = \sum_{i} \Phi(f_i),$$
(17)

where $\hat{u}' = \hat{u} - \overline{\hat{u}}$ and $\hat{T}' = \hat{T} - \overline{\hat{T}}$. It shows that at $Ra = 1.83 \times 10^8$ the fluctuations are characterized by several peaks at a certain frequency, and the primary frequency is around $f_1 \approx 0.5$. This shear-driven Kelvin–Helmholtz type instability is the primary instability claimed by Janssen and Henkes, which takes place in a jet-like fluid layer in the detached region and is characterized by the low frequency. Different from the Boussinesq convection, in which the primary instability happens in the detached region for both top left corner and bottom right corner simultaneously, the first instability of the compressible natural convection appears only at the bottom right corner near the cold wall.

The second simulation case is for $Ra = 3.0 \times 10^8$. As shown in Fig. 5(b), fluctuations start to appear along the hot wall in addition to the cold wall corner. Small vortices are generated along the hot wall boundary; they travel along the hot wall and then turn horizontal and eject to the detached region. The instability near the cold wall still concentrates in the detached region. Two large eddies are generated and break into smaller eddies. Two monitoring points are chosen for the

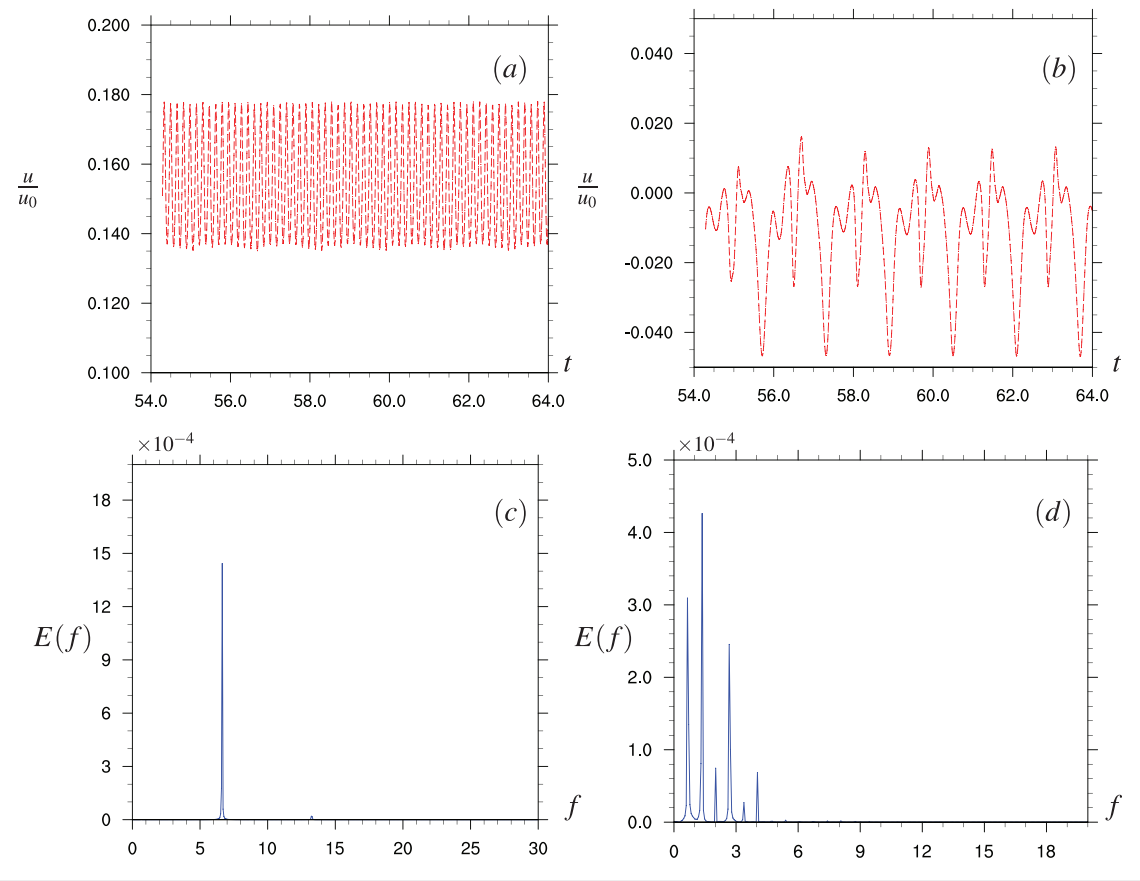


FIG. 8. Time trace of velocity $\frac{u(t)}{u_0}$ (top) and their spectrum of fluctuation velocity (bottom) E(f) at monitoring points with $Ra = 3.0 \times 10^8$. (a) and (c) for point (0.85, 0.025)L, (b) and (d) for point (0.07, 0.85)L.

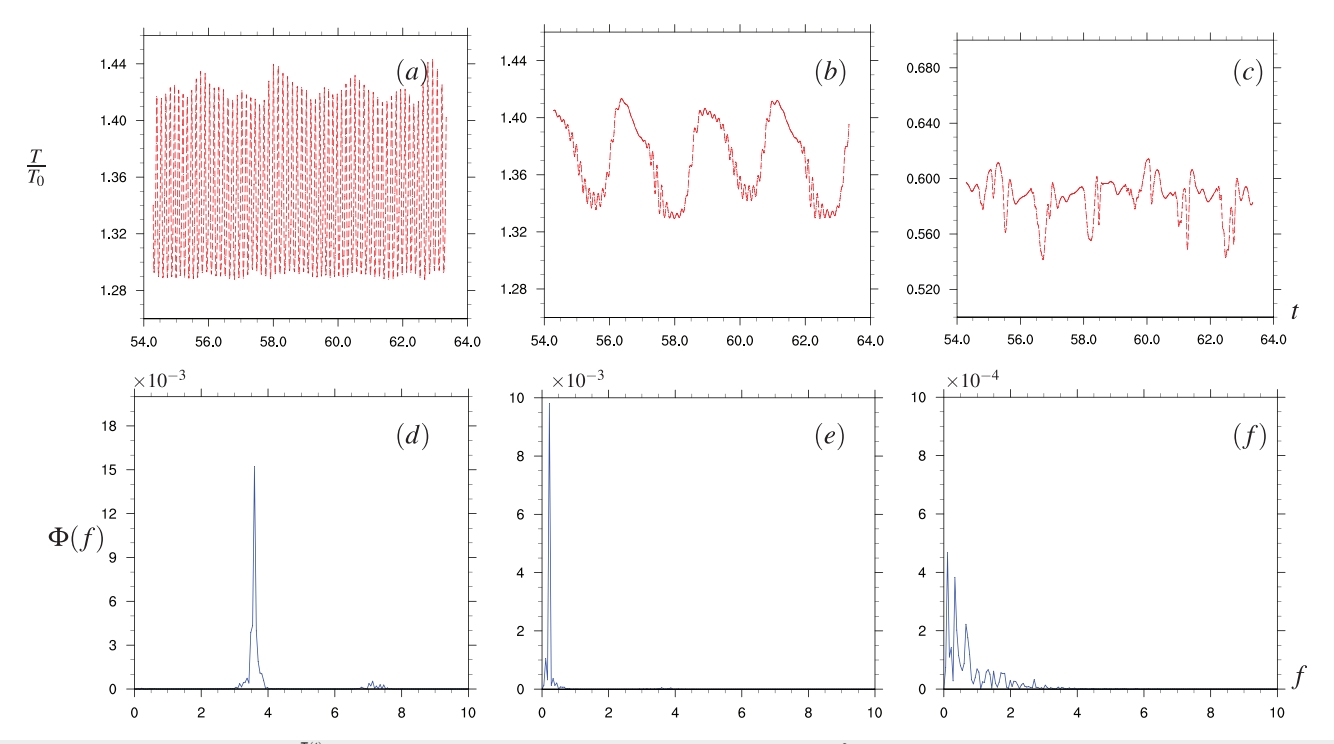


FIG. 9. Time trace of temperature $\frac{T(t)}{T_0}$ (top) and their spectrum $\Phi(f)$ (bottom) with $Ra = 5.0 \times 10^8$. (a) and (d) for point (0.9, 0.025)L, (b) and (e) for point (0.8, 0.2)L, (c) and (f) for point (0.05, 0.95)L.

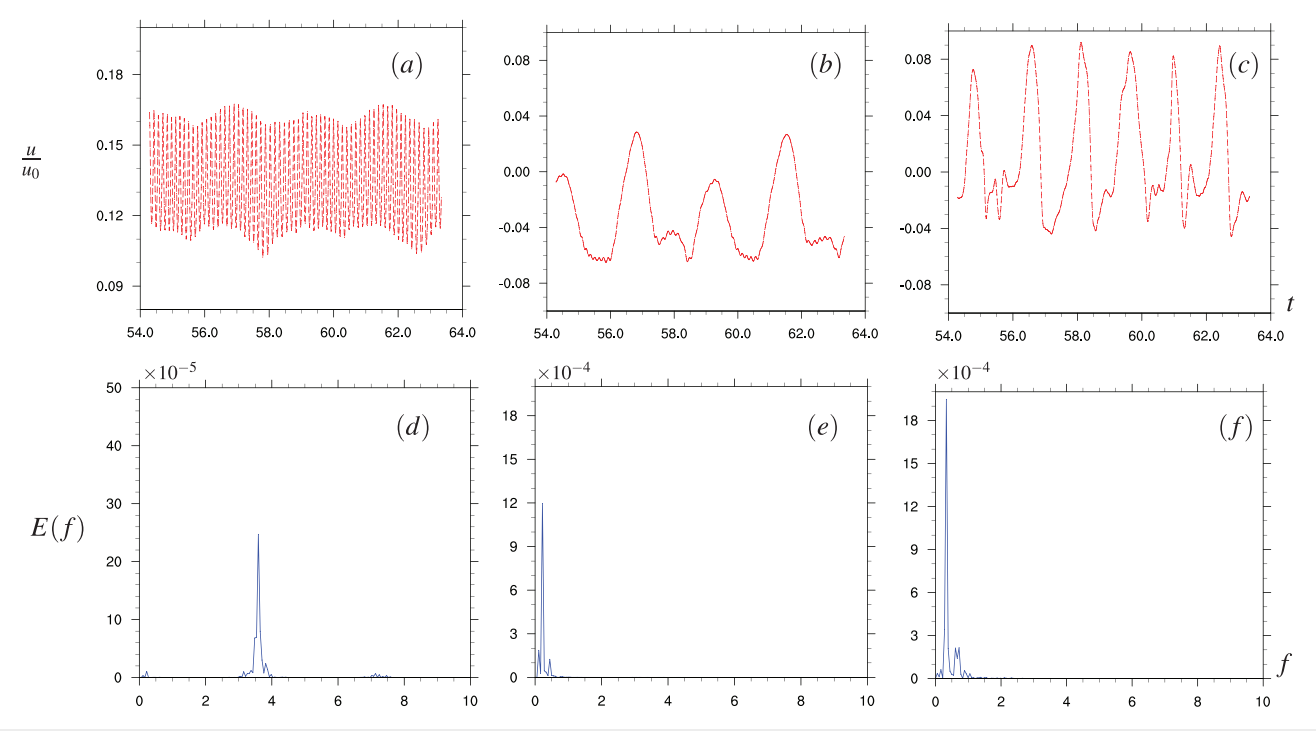


FIG. 10. Time trace of velocity $u(t)/u_0$ (top) and their spectrum of fluctuation velocity E(f) with $Ra = 5.0 \times 10^8$. (a) and (d) for point (0.9, 0.025)L, (b) and (e) for point (0.8, 0.2)L, (c) and (f) for point (0.05, 0.95)L.

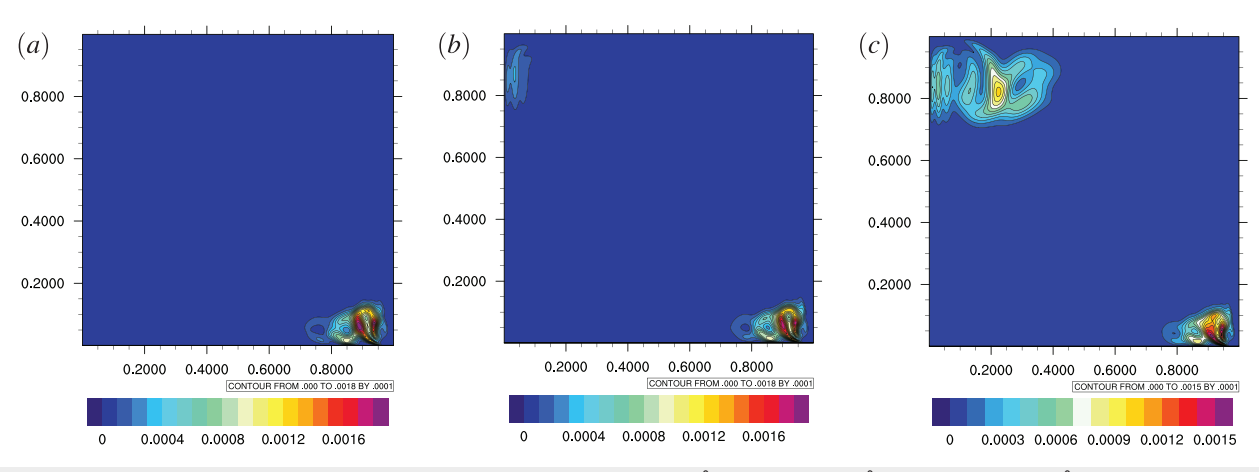


FIG. 11. Turbulent kinetic energy contours for (a) $Ra = 1.83 \times 10^8$, (b) $Ra = 3.0 \times 10^8$, and (c) $Ra = 5.0 \times 10^8$.

time trace of temperature and velocity: one along the hot wall boundary layer (0.85, 0.025)L and one in the detached region of cold wall corner (0.07, 0.85)L. Figures 7(a) and 7(b) show the time trace of temperature at these monitoring points and its spectrum, respectively; the oscillations near the hot wall are characterized by a single peak which implies a periodic flow. It is worth pointing out that the hot wall boundary layer oscillation is at a much higher frequency ($f_2 \approx 6$) than the primary oscillations in the cold wall detached region. It is obvious that the instability of the hot wall boundary layer is distinct from the primary instability; it is characterized by small vortices and higher frequency. Figures 8(a) and 8(b) display the vertical velocity time trace $u(t)/u_0$ at monitoring points, the fluctuation amplitude for the hot wall boundary layer $\left|\frac{\Delta u}{u_0}\right| \approx 0.04$, and the spectrum concentrates at a single frequency f_2 . For the monitoring point at cold wall detached region, the fluctuation amplitude of the velocity time trace is $\left|\frac{\Delta u}{u}\right| \approx 0.06$, and the spectrum locates at lower frequencies. This traveling wave instability taking place in the hot wall boundary layer starts to appear at a slightly higher Rayleigh number after the first instability in the cold wall detached region. For this Rayleigh number, the boundary layer along the cold wall is still stable. The second instability does not take place at the cold isothermal wall boundary layer. This phenomenon is consistent with the previous studies that the heating decreases the boundary layer instability, while cooling increases the boundary layer instability.

For the third case at $Ra = 5.0 \times 10^8$, more vortices are generated in the detached region near the cold wall as shown in Fig. 5(c). The number of vortices along the hot wall boundary layer also increases. After these eddies reach the top horizontal walls, they turn into the horizontal direction and travel along the top adiabatic wall.

TABLE IV. Percentage of TKE in the cold region.

Ra	1.83×10^{8}	3.0×10^{8}	5.0×10^{8}
$\frac{\int_{cold} TKEdV}{\int TKEdV}$	97.43%	81.55%	32.41%

Three monitoring points are chosen for the time trace of temperature and velocity: one along the hot wall boundary layer (0.9, 0.025)L, one at the detached region of the top adiabatic wall (0.8, 0.2)L, and one in the detached region of cold wall corner (0.05, 0.95)L. Figures 9(a) and 9(d) show the time trace and spectrum of the monitoring point at the hot wall boundary. Instead of a single peak at a frequency $f \approx 4$, the oscillations also take place near this primary frequency, and there is another smaller amplitude spike at an even higher frequency $f \approx 7$. The time trace of the top wall detached region is shown in Figs. 9(b) and 9(e). The temperature spectrum is characterized by a single peak at $f_1 \approx 0.5$, which indicates that the top wall detached region is dominated by the primary instability. For the detached region near the cold wall, there is no evident periodic behavior and the spectrum spread out from the low frequency to high frequency. The time trace of vertical velocity and their spectrum are shown in Fig. 10. The fluctuation amplitude at the bottom wall detached region reaches $\left|\frac{\Delta u}{u_0}\right| \approx 0.12$, which approximates three times of the velocity fluctuation amplitude of the hot wall boundary layer.

The turbulent kinetic energy (TKE) $TKE = \frac{1}{2}(\overline{u'u'} + \overline{v'v'})/(u_0^2Pr)$ is computed, where velocity component $u' = u - \overline{u}$ is the difference between the instantaneous and the time-averaged velocity. Here (and also in Fig. 12), Pr is added as in the literature and $u_0\sqrt{Pr}$ is used as the reference velocity scale. This statistic is averaged over approximately 20 eddy turnover times after the flow reaches statistical stationarity. The eddy turnover time is defined as $\frac{4L}{u_0/3}$, where $u_0/3$ approximates the maximum flow velocity and 4L is the maximum flow path. The TKE contours for different Rayleigh numbers are shown in Fig. 11. These contours clearly demonstrate the development of the instability. At the lowest Rayleigh number $Ra = 1.83 \times 10^8$, the

TABLE V. Parameters for the simulation of compressible unsteady natural convection.

Ra	Pr	γ	3	Ма
$1.5 \sim 5.0 \times 10^9$	0.71	1.4	0.6	$0.1 \sim 0.2927$
$p_0 (\mathrm{kg/ms^2})$	$T_0(K)$	$R \left(m^2 / s^2 K \right)$	$g (m/s^2)$	μ_0
101 325.0	600.0	287	g(Ma)	$\mu(Ra)$

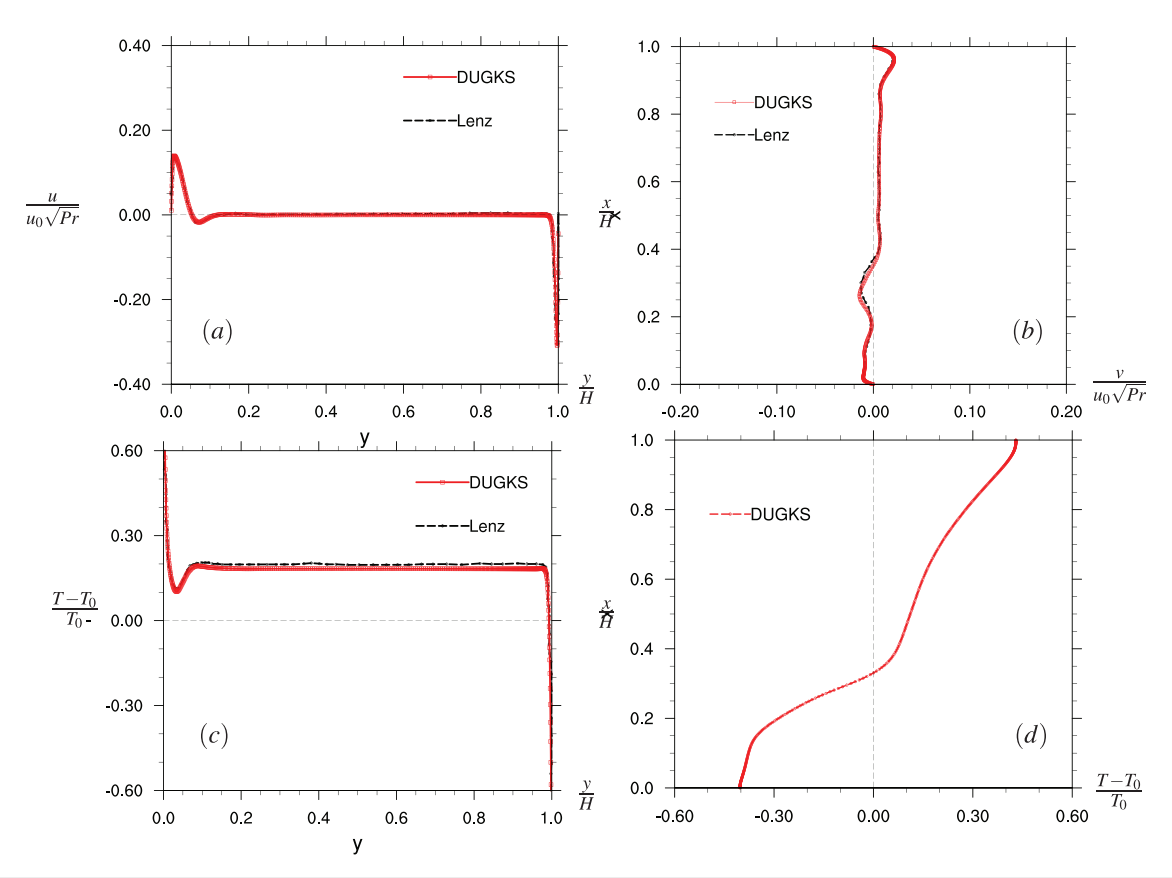


FIG. 12. (a) Vertical velocity and (c) temperature distribution at the mid-height x=0.5L; (b) horizontal velocity and (d) temperature distribution at the mid-width y=0.5L for $Ra=5.0\times10^9$, $\varepsilon=0.6$.

TKE only concentrates at the detached region near the cold wall, which corresponds to the primary instability characterized by large amplitude and low-frequency oscillations. With $Ra = 3.0 \times 10^8$, moderate values of TKE appear at the downstream of the hot wall

boundary layer due to the small magnitude oscillations inside the vertical boundary layer. When the Rayleigh number reaches $Ra = 5.0 \times 10^8$, the instability in the detached region near the top wall becomes significant, and its magnitude is larger than the TKE in the

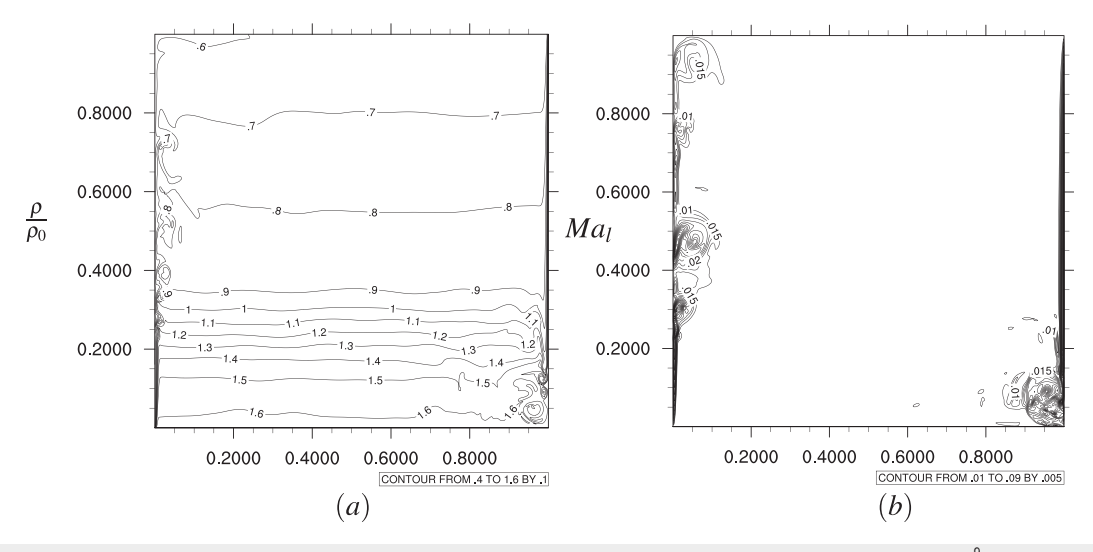


FIG. 13. (a) Density contour and (b) local Mach number contour for compressible natural convection with $Ra = 5.0 \times 10^9$, $\varepsilon = 0.6$.

hot wall boundary layer. Table IV summarizes the percentage of TKE in cold region $x = [0:L], y = \left[\frac{L}{2}:L\right]$, at $Ra = 1.83 \times 10^8$ almost all TKE concentrates in the cold region, which comes from the primary instability in the detached region. At $Ra = 3.0 \times 10^8$, the instability in the hot wall boundary layer starts to contribute to the TKE, but due to its small magnitude oscillation, the majority of TKE still comes from the primary instability. At $Ra = 5.0 \times 10^8$, with the help of instability in the detached region near the top wall, TKE of the hot wall region exceeds TKE of the cold region.

Based on the analysis above, we can reach a conclusion that there are two types of instability. The primary instability first appears in the detached region near the cold wall which is characterized by large-magnitude and low-frequency oscillations. The second instability inside the hot wall boundary layer appears at a slightly higher Rayleigh

number and has the feature of small-magnitude and high-frequency oscillations. The instability in the detached region near the top adiabatic wall takes place when more eddies turn horizontal due to the top wall. One major characteristic of the instability for the compressible natural convection is that it is highly asymmetric. Two types of instability do not take place simultaneously for the hot wall and cold wall region. For the Rayleigh number range $Ra = 1.83 \sim 5.0 \times 10^8$, the second instability is not observed in the cold wall boundary layer.

C. Compressible convection at higher Rayleigh number

To investigate the flow feature of compressible natural convection at high Rayleigh numbers and the transition to turbulence, a set of

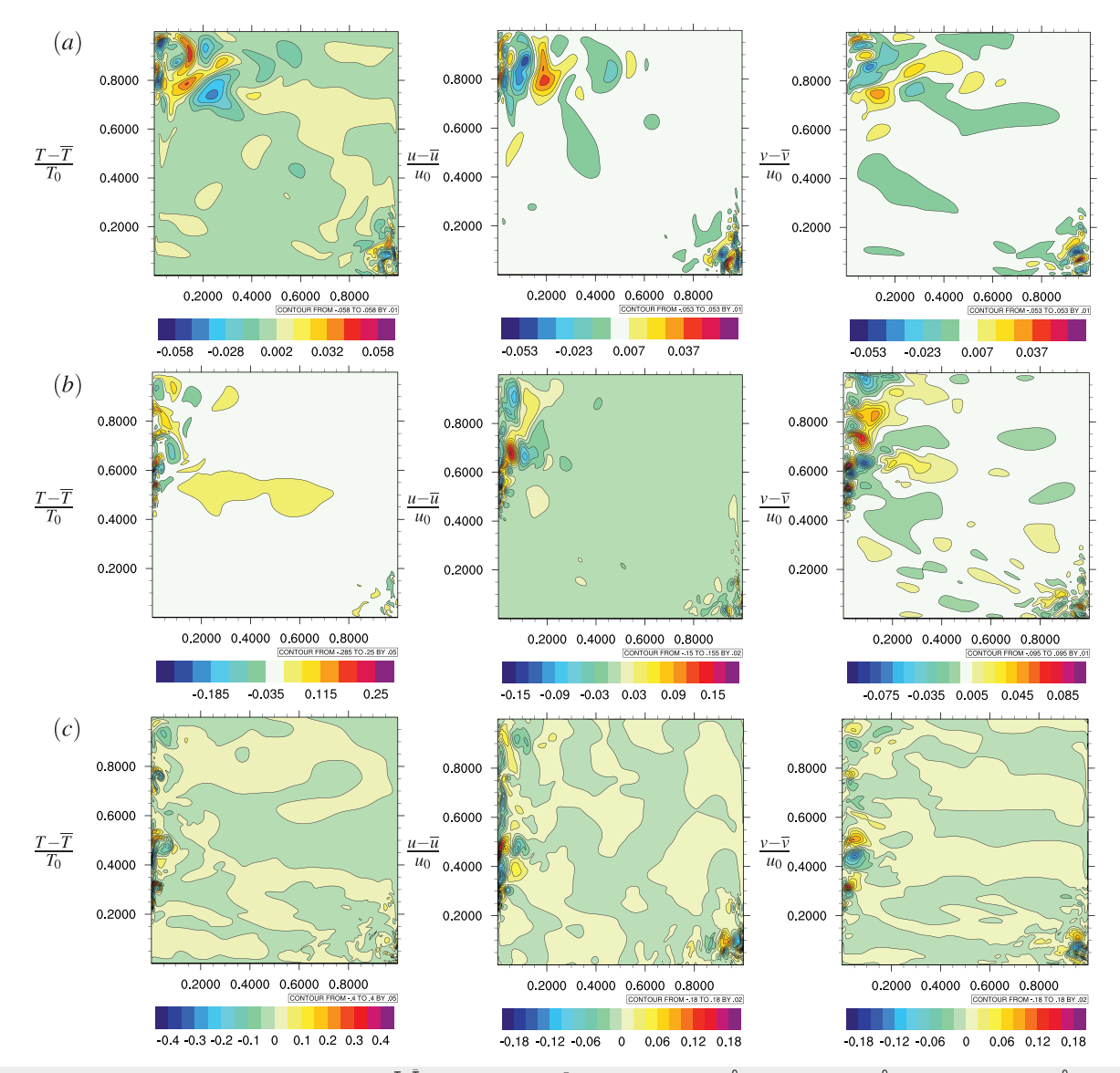


FIG. 14. Instantaneous fluctuation temperature $\frac{T-\overline{I}}{T_0}$ and velocity field $\frac{u-\overline{u}}{u_0}$ for (a) $Ra=1.5\times10^9$, (b) $Ra=3.0\times10^9$, and (c) $Ra=5.0\times10^9$.

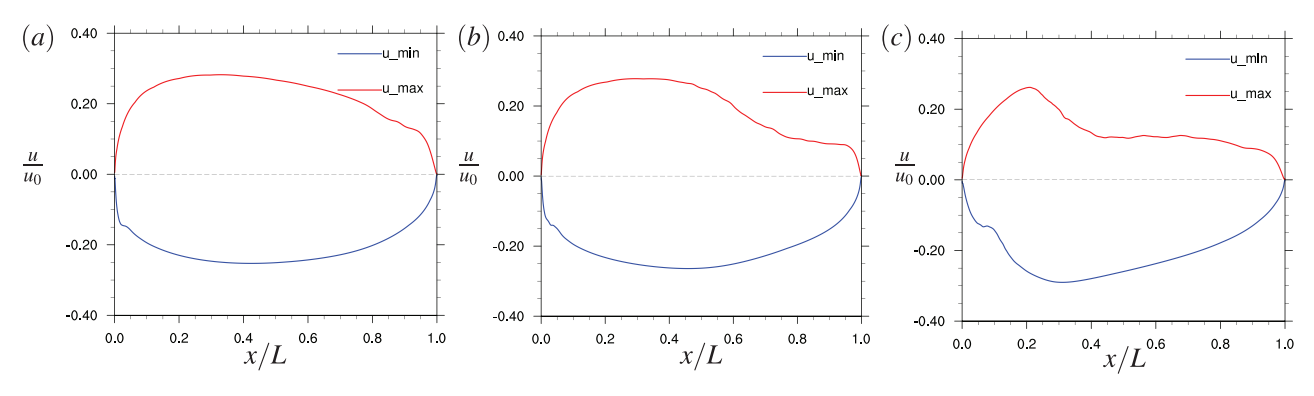


FIG. 15. The variation of maximum/minimum vertical velocity with the height on the hot/cold wall at (a) $Ra = 1.5 \times 10^9$, (b) $Ra = 3.0 \times 10^9$, and (c) $Ra = 5.0 \times 10^9$

simulations up to $Ra = 5.0 \times 10^9$ are performed and analyzed. Fine resolution of 360×360 with $\Delta x_{\min} = 4.1154 \times 10^{-4} L$ is used to resolve the steep temperature and velocity gradient near the boundary. Table V shows the parameter setting for these simulations. Figure 12 shows the time-averaged temperature and velocity profiles for the case $Ra = 5.0 \times 10^9$. Our results reach an excellent agreement with GKS results of Lenz et al.²⁹ The statistics are averaged over approximately 75 eddy turnover times, namely, a duration of $75 \times \frac{4L}{u_0/3}$. We can observe that the flow is highly asymmetric at this Rayleigh number; the cold wall boundary layer is extremely thin, while the fluid near the hot wall is expanded. The horizontal velocity profile at the mid-width is relatively complex. The maximum velocity near the top wall is adjacent to the wall, while the maximum velocity for the bottom part is near the cavity center. The temperature stratification in the cavity center can be distinguished into two parts with a different slope. Another feature of the compressible natural convection at high Rayleigh number is that the spatially averaged mean temperature \bar{T} is higher than the reference temperature T_0 due to the expansion of the hot fluid. Figure 13 shows the instantaneous density contour and local Mach number $Ma_l = \frac{\sqrt{u^2 + v^2}}{\sqrt{\sqrt{RT}}}$ contour. The maximum value of the local

Mach number for this case remains small, $Ma_{l,\max} \approx 0.1$. Thus, the compressible effect as seen from the density change is due to the large temperature change.

Figure 14 shows the instantaneous temperature and velocity magnitude contours. We can observe that at $Ra = 1.5 \times 10^9$, small vortices are generated along the downstream of the hot wall and cold wall boundary layer, and large vortices appear at the top wall detached region. At $Ra = 3.0 \times 10^9$, vortices at the hot wall start to appear at x = 0.4L and travel along the isothermal wall. Fluctuations in the top wall detached region seem to be depressed. With the highest Rayleigh number 5.0×10^9 , the vortices start to appear at $x \approx 0.2L$, which is distinct from small Rayleigh number case or Boussinesq-type convection. While for the cold wall, fluctuations occur at the cold wall corner. Figure 15 shows the maximum/minimum vertical velocity as a function of the height on the hot/cold wall for three Rayleigh numbers. Together with Table III, we can observe that with the increase in the Rayleigh number, the magnitude of the minimum vertical velocity along the cold wall becomes larger than that of the cold wall. Furthermore, the location of the maximum vertical velocity along the hot wall moves downwards. For cases $Ra = 1.5 \times 10^9$ and

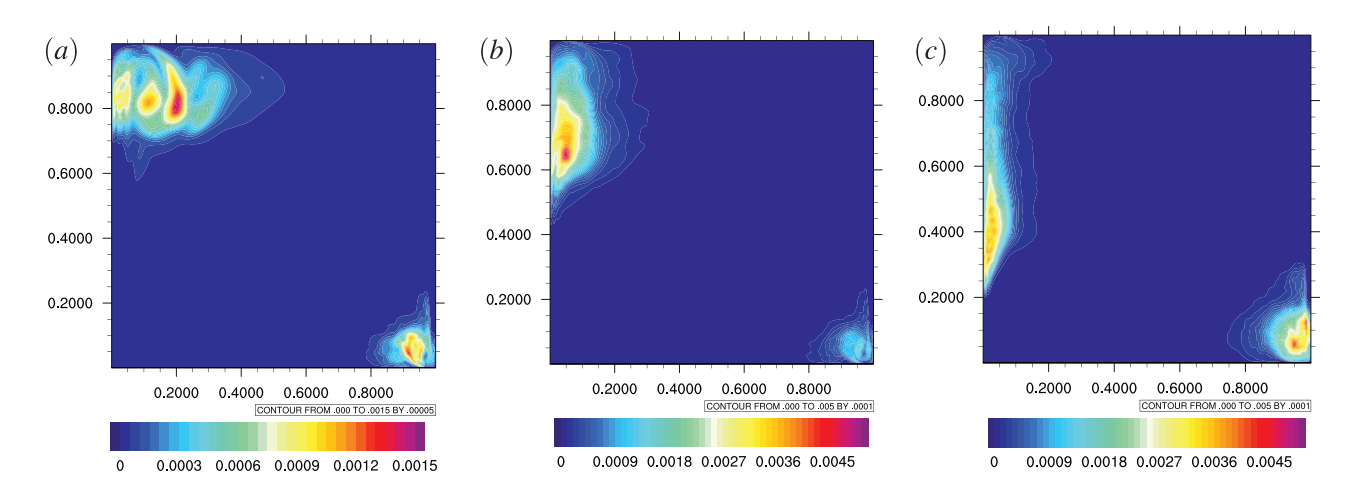


FIG. 16. Turbulent kinetic energy contours for (a) $Ra = 1.5 \times 10^9$, (b) $Ra = 3.0 \times 10^9$, and (c) $Ra = 5.0 \times 10^9$

 $Ra = 3.0 \times 10^9$, the vertical velocity reaches its maximum value near the height x = 0.4L. For the case $Ra = 5.0 \times 10^9$, the location moves down to $x \approx 0.2L$. The vertical velocity reaches its maximum value before the vortices start to be generated. It is worth pointing out that the upward vertical velocity reaches its maximum at the upstream in the hot wall thermal boundary layer and then decreases as the boundary layer expands, while for the cold wall, the downward vertical velocity reaches its maximum at the downstream of the cold wall thermal boundary layer. Therefore, the fluid jet hitting the bottom corner region of the cold wall tends to have a larger speed than that of the hot wall fluid jet. This may explain why the cold wall detached region is dominated by the primary instability, while for the hot wall detached region, the primary instability is depressed with the increase in the Rayleigh number.

Turbulent kinetic energy contours are shown in Fig. 16; these contours clearly demonstrate the development of the fluctuations at different Ra numbers. At the smallest Rayleigh number, the maximum fluctuation locates at the top wall detached region. With the increase in the Rayleigh number, the instability in the detached region is depressed, the center of the TKE moves toward the upstream of the isothermal wall. At $Ra = 5.0 \times 10^9$, the TKE distributes along the hot wall, and center on $x \approx 0.4L$, there is no obvious TKE on the top wall

detached region, while for the cold wall region, TKE still concentrates on the cold wall corner. The TKE of the cold wall region is 36.82% of the overall TKE. It is worth noticing that the values of TKE along the hot wall and the cold wall are on the same magnitude for this high Rayleigh number case.

Two monitoring points are chosen at the hot wall (0.4, 0.025)Land cold wall (0.1, 0.95)L based on the TKE contour of $Ra = 5.0 \times 10^9$. Figure 17 shows the temperature trace at the monitoring points. There is no obvious periodic behavior of the signal at this high Rayleigh number. The temperature variation is significant $\left|\frac{\Delta T}{T_0}\right| \approx 0.3$ for both hot wall and cold wall. The spectrum spreads out from low frequency to high frequency, which indicates the flow reaches the turbulent flow regime. Figure 18 shows the vertical velocity time trace. The spectrum of fluctuation velocity E(f) of the hot wall monitoring point peaks at frequency $f \approx 3$, while the spectrum of the cold wall monitoring points peak near the $f \approx 0$. The velocity signal near the hot wall still oscillates at a higher frequency than the signal of the cold wall. From the statistics and analysis above, we show that with the increase in the Rayleigh number, the instability in the detached region is depressed. The traveling wave instability inside the boundary layer gradually becomes turbulent; the oscillations spread to all frequencies.

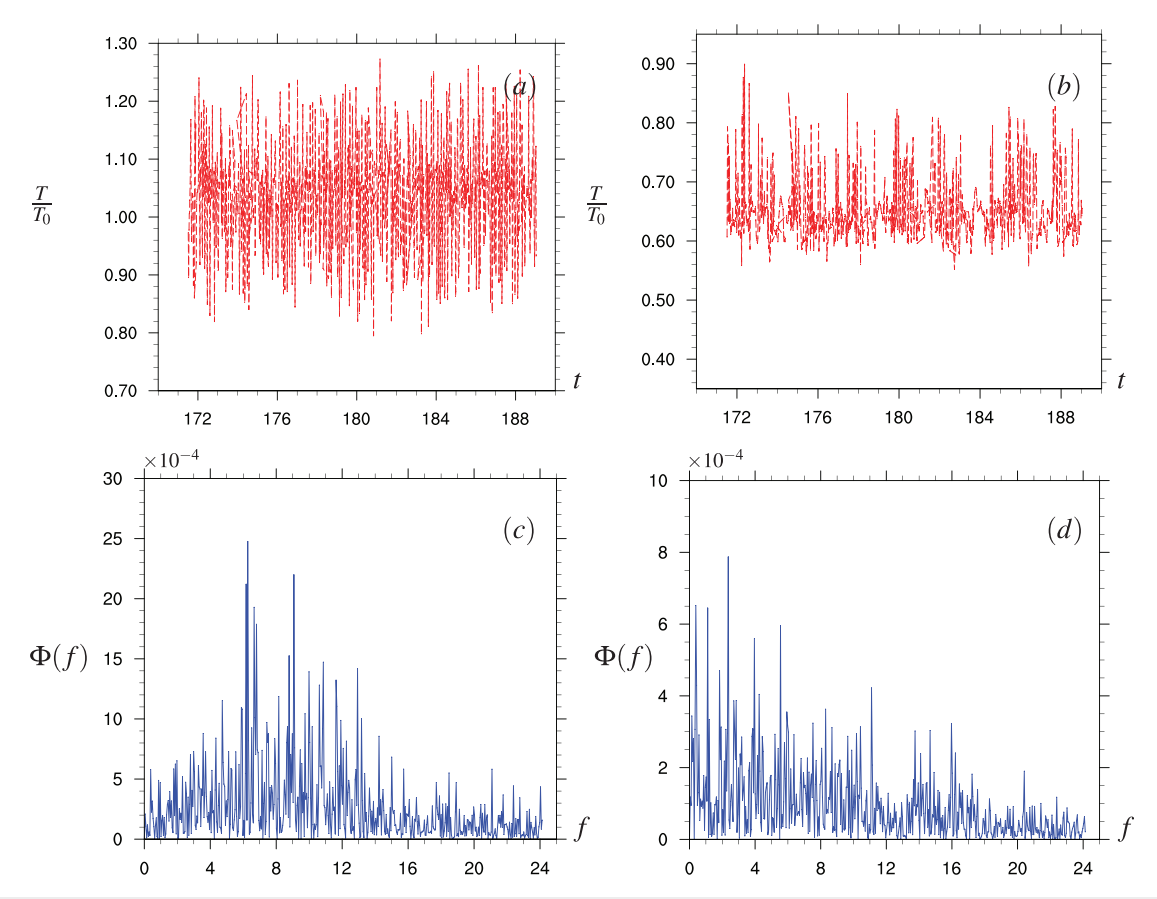


FIG. 17. Time trace of temperature $\frac{T}{T_0}$ and its spectrum $\Phi(f)$ at monitoring points with $Ra = 5.0 \times 10^9$. (a) and (c) for point (0.4, 0.025)L, (b) and (d) for point (0.1, 0.95)L.

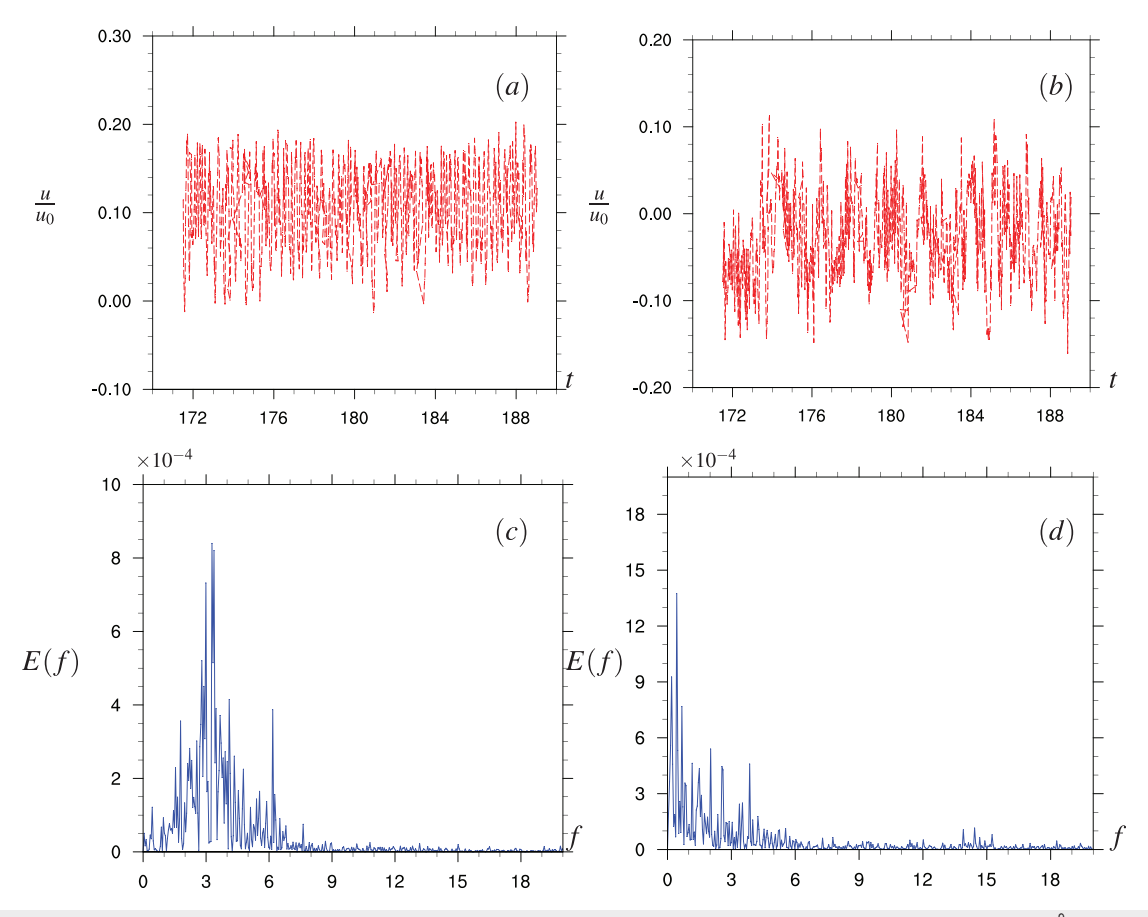


FIG. 18. Time trace of velocity $u(t)/u_0$ (top) and their frequency spectrum (bottom) E(f) of velocity at monitoring points with $Ra = 5.0 \times 10^9$. (a) and (c) for point (0.4, 0.025)L, (b) and (d) for point (0.1, 0.95)L.

Figure 19 shows the Nusselt–Rayleigh dependence of the Rayleigh number range we studied. Compared to the Boussinesq cases, the Nusselt number of the compressible natural convection is slightly lower. Our results agree well with finite-difference results of Wang *et al.*³⁵ They solved the low-Mach-number equations and provided Ra–Nu correlation for the Rayleigh number range $1.0 \times 10^5 \le Ra \le 1.0 \times 10^9$. The reasons for smaller Nusselt numbers for the non-Boussinesq cases are perhaps due to (1) smaller local effective Rayleigh number as a result of the increased viscosity and increased conductivity with temperature, and (2) compressibility which tends to expand the thermal boundary layer near the hot wall. The Nu–Ra dependence for the case $\varepsilon = 0.6$ can be fitted by an empirical relation,

$$\overline{Nu} = (0.2714 \pm 0.0092) Ra^{0.2542} \quad (1.83 \times 10^8 \le Ra \le 5.0 \times 10^9),$$
(18)

where the relative error between the time-averaged mean Nusselt number and the *Nu–Ra* fitting is shown in Table VI, and the maximum relative error is around 3.3%.

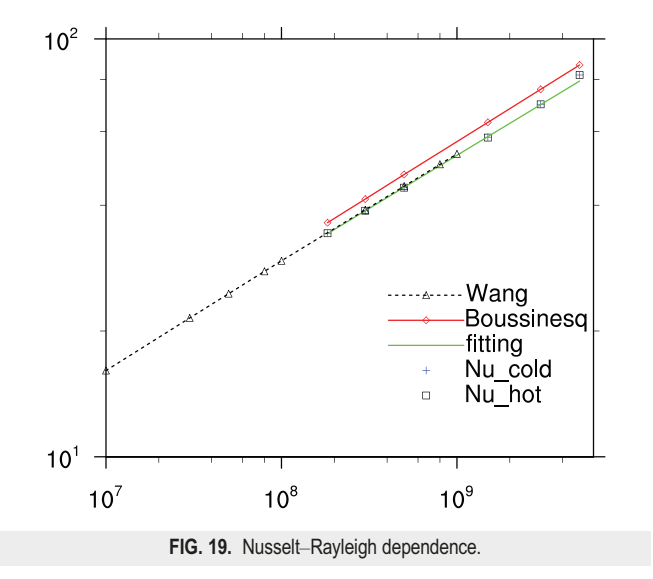


TABLE VI. Time-averaged mean Nusselt number and Nu-Ra fitting. The relative error between Nu_{hot} and $Nu_{fitting}$ is defined as $Err = (Nu_{hot} - Nu_{fitting})/Nu_{hot}$.

Ra	1.83×10^{8}	3.0×10^{8}	5.0×10^{8}	1.5×10^{9}	3.0×10^{9}	5.0×10^{9}
Nu_{hot}	34.2718	38.8017	44.0626	58.0636	69.7355	81.9505
Nu _{fitting}	34.1920	38.7698	44.1457	58.3677	69.6136	79.2622
Err(%)	0.2328	0.0822	-0.1886	-0.5237	0.1748	3.2804

IV. SUMMARY AND CONCLUSIONS

In this study, we investigated the development of unsteady natural convection in an air-filled square cavity using an improved discrete unified-gas kinetic scheme (DUGKS). The coupled double-distribution function model with the BGK collision operator is employed. An extra source term is introduced to adjust the Prandtl number. This source term only contributes to the heat flux term without changing the continuity and momentum equations. The fully compressible Navier–Stokes equations are recovered by the current scheme.

We have performed a series of two-dimensional simulations of compressible natural convection in an air-filled differentially heated square cavity for the Rayleigh number in the range of $10^7 \sim 10^9$. We first showed that the critical Rayleigh number for the transition from steady to unsteady flow is between $4.05 \times 10^7 < Ra_{cr} < 4.25 \times 10^7$. To investigate the instability mechanism, we provide instantaneous fluctuation contours, temperature and velocity signals at monitoring points, turbulent kinetic energy contours, and energy spectra of fluctuations. We have shown that there are two major types of instability; the first instability appears in a jet-like fluid layer in the detached region near the cold wall. This shear-driven, Kelvin-Helmholtz type instability is characterized by low-frequency oscillations with a nondimensional frequency of about $f_1 \approx 0.5$. The second instability is the boundary layer instability which takes place inside the hot wall boundary layer along the vertical isothermal wall at a slightly higher Rayleigh number. This instability is featured by high-frequency oscillation with a dimensionless frequency of about 6.0 and small vortices. The crucial difference between the instability of compressible natural convection and Boussinesq-type convection is that the instability is highly asymmetric about the cavity center and asynchronous appearance of the instabilities for the compressible case: (1) The primary instability first appears at the detached region of the cold wall at a lower Rayleigh number. When the Rayleigh number further increases, the primary instability starts to take place in the detached region of the hot wall. (2) For the Rayleigh number range we studied, the boundarylayer instability is only observed along the hot wall. (3) When the Rayleigh number further increases, the first instability in the detached region is depressed, and the traveling wave instability inside the boundary layer starts to appear at a lower height. The oscillations eventually become nonperiodic and the flow becomes weakly turbulent.

Despite the effort we make here, there is still much work to be done. The instability of compressible natural convection can be affected by a large range of system parameters such as the cavity aspect ratio, Prandtl number, temperature difference, etc. Systematic studies are needed to investigate the dependence of instability on these different controlling parameters. As the turbulence is essentially three-

dimensional, three-dimensional high Rayleigh number convection simulation is needed for the future work.

ACKNOWLEDGMENTS

This work has been supported by the Southern Marine Science and Engineering Guangdong Laboratory (Guangzhou) (Grant No. GML2019ZD0103), the National Natural Science Foundation of China (NSFC Award Nos. 91852205, 91741101, and 11961131006), NSFC Basic Science Center Program (Award No. 11988102), the U.S. National Science Foundation (Nos. CNS-1513031 and CBET-1706130), the National Numerical Wind Tunnel program, Guangdong Provincial Key Laboratory of Turbulence Research and Applications (No. 2019B21203001), Guangdong-Hong Kong-Macao Joint Laboratory for Data-Driven Fluid Mechanics and Engineering Applications (No. 2020B1212030001), and Shenzhen Science & Technology Program (Grant No. KQTD20180411143441009). Computing resources are provided by the Center for Computational Science and Engineering of Southern University of Science and Technology and by National Center for Atmospheric Research (No. CISL-UDEL0001).

APPENDIX: BOUNDARY CONDITION

In our current configuration, we have two distribution functions $g(\xi_\alpha, \mathbf{x}, t)$ and $h(\xi_\alpha, \mathbf{x}, t)$; subscript α represents the discrete velocity. No-slip boundary condition $(\mathbf{u}=0)$ is applied for all walls; two vertical walls are at a fixed temperature (T_w) and horizontal walls are adiabatic $\left(\frac{\partial T}{\partial x}=0\right)$. A systematic approach of deriving boundary condition is developed; details of derivation are shown in our other paper. In general, the distribution functions g and h can be expanded to the order of $O(\tau)$ by Chapman–Enskog expansion. Then the time and spatial derivatives of equilibrium distributions $\frac{\partial g^{eq}}{\partial t}$, $\frac{\partial g^{eq}}{\partial x_j}$, $\frac{\partial g^{eq}}{\partial \xi_j}$ can be written out with the help of the Maxwellian distributions in Eq. (5). Using the Euler equations to remove all the time derivatives of hydrodynamic variables $\frac{\partial p}{\partial t}$, $\frac{\partial u_i}{\partial t}$, $\frac{\partial T}{\partial t}$, we can obtain the final form for the structure of the distribution function as follows:

$$g = g^{eq} \begin{cases} 1 - \frac{\tau c_i c_j}{RT} \frac{\partial u_i}{\partial x_j} + \tau \left[\frac{c^2}{(K+3)RT} + \frac{\tilde{K}}{K+3} \right] \frac{\partial u_j}{\partial x_j} \right\} + \mathcal{O}(\tau^2), \\ -\tau c_j \frac{\partial T}{\partial x_j} \left(\frac{c^2}{2RT^2} - \frac{D+2}{2T} \right) \end{cases}$$

$$(A1a)$$

$$h = h^{eq} \begin{cases} 1 - \frac{\tau c_i c_j}{RT} \frac{\partial u_i}{\partial x_j} + \tau \left[\frac{c^2}{(K+3)RT} + \frac{\tilde{K}+2}{K+3} \right] \frac{\partial u_j}{\partial x_j} \\ -\tau c_j \frac{\partial T}{\partial x_j} \left(\frac{c^2}{2RT^2} - \frac{D}{2T} \right) \end{cases}$$

where equilibrium distribution functions g^{eq} , h^{eq} can be expanded using Hermite expansion. Then, we can derive the following kinetic boundary conditions based on the physical boundary conditions.

The bounce-back expression of distribution function can be expressed as

$$g(\xi_{a,j}) = g(\xi_{\bar{a},j}) - \tau W_a \rho_w \frac{\xi_{a,j}}{T_0} \frac{\partial T}{\partial x_j}$$

$$\begin{cases} \left(\frac{\xi_a^2}{RT_0} - D - 2\right) \\ \frac{1}{2}(\theta - 1) \left[\frac{\xi_a^4}{(RT_0)^2} - 2(D+3)\frac{\xi_a^2}{RT_0} + (D+2)^2\right] \\ \frac{1}{8}(\theta - 1)^2 \left[\frac{\xi_a^6}{(RT_0)^3} - (3D+14)\frac{\xi_a^4}{(RT_0)^2} + (D+4)(3D+10)\frac{\xi_a^2}{(RT_0)} - (D+2)^2(D+4) \right] \\ + \mathcal{O}(\tau^2, Ma^5), \end{cases}$$

$$(A2)$$

where $\theta = \frac{T_w}{T_0}$, ρ_w , T_w are the density and temperature on the wall, $\xi_{a,j}$ denotes the particles bouncing back from the wall, and $\xi_{\bar{a},j} = -\xi_{a,j}$. The temperature gradient $\frac{\partial T}{\partial x_j}$ is approximated with values at previous time step by finite-difference. The above boundary condition can be viewed as the improved bounce-back retaining the $\mathcal{O}(\tau)$ terms. For adiabatic walls, we apply the following expression to the distribution function:

$$h(\xi_{a,j}) = h(\xi_{\bar{a},j}) - \tilde{K}\rho R\tau W_a \xi_{a,j} \frac{\partial T}{\partial x_j} \left\{ \left(\frac{\xi_a^2}{RT_0} - D \right) + \frac{1}{2} (\theta - 1) \left[\frac{\xi_a^4}{(RT_0)^2} - 2(D+1) \frac{\xi_a^2}{RT_0} + D^2 \right] \right\} + 2W_a \frac{2(1-Pr)}{\sqrt{RT_0}} \frac{\xi_a \cdot \mathbf{q}}{\sqrt{RT_0}} + \mathcal{O}(\tau^2, Ma^3),$$
(A3)

where $\tilde{K} \equiv (K+3-D)$, and \boldsymbol{q} is the heat flux at the wall. For the top and bottom adiabatic walls, $q_x=0$ is imposed. Heat flux in tangential direction q_y can be approximated by the heat flux value at previous time step $q_y^{(n-1)} = \frac{1}{2} \int c_y (c^2 g^{(n-1)} + h^{(n-1)}) d\boldsymbol{\xi}$. For isothermal walls, we have

$$\begin{split} h(\xi_{a,j}) &= -h(\xi_{\bar{a},j}) + 2W_a\tilde{K}p \left[1 + \frac{1}{2}(\theta - 1) \left(\frac{\xi_a^2}{RT_0} - D \right) \right] \\ &+ 2\tau W_a\tilde{K}p \frac{\partial u_j}{\partial x_j} \\ &\times \left[\begin{array}{c} (2 - \theta) \frac{\xi_a^2}{(K+3)RT_0} + \frac{\tilde{K}+2}{K+3} \\ &+ \frac{1}{2}(\theta - 1) \left(\frac{\xi_a^2}{RT_0} - D \right) \left(\frac{\xi_a^2}{(K+3)RT_0} + \frac{\tilde{K}+2}{K+3} \right) \right] \\ &+ 2\tau W_a\tilde{K}p \frac{\xi_{a,i}\xi_{a,j}}{RT_0} \frac{\partial u_i}{\partial x_j} \left[\theta - 2 - \frac{1}{2}(\theta - 1) \left(\frac{\xi_a^2}{RT_0} - D \right) \right] \\ &+ \mathcal{O}(\tau^2, Ma^3), \end{split} \tag{A4}$$

where $T_w = T_h$ or $T_w = T_c$ is applied at hot and cold wall respectively. The velocity gradient $\frac{\partial u_i}{\partial x_i}$, $\frac{\partial u_i}{\partial x_j}$ is calculated by finite-difference using the values from last time step. It is worth pointing out that the expressions for the boundary condition implementations above are derived based on the Chapman–Enskog analysis, which implies that the boundary treatment is consistent with the Navier–Stokes–Fourier equations.

DATA AVAILABILITY

The data that support the findings of this study are available from the corresponding author upon reasonable request.

REFERENCES

¹J. W. Elder, "Laminar free convection in a vertical slot," J. Fluid Mech. 23, 77–98 (1965).

²G. D. Mallinson and G. D. V. Davis, "Three-dimensional natural convection in a box: A numerical study," J. Fluid Mech. 83, 1–31 (1977).

³J. R. Lee, "On the three-dimensional effect for natural convection in horizontal enclosure with an adiabatic body: Review from 2D results and visualization of 3D flow structure," Int. Commun. Heat Mass Transfer 92, 31–38 (2018).

⁴S. Pandey, Y. G. Park, and M. Y. Ha, "An exhaustive review of studies on natural convection in enclosures with and without internal bodies of various shapes," Int. J. Heat Mass Transfer 138, 762–795 (2019).

⁵D. Lohse and K. Q. Xia, "Small-scale properties of turbulent Rayleigh-Bénard convection," Annu. Rev. Fluid Mech. 42, 335–364 (2010).

⁶R. J. A. Janssen and R. A. W. M. Henkes, "Influence of Prandtl number on instability mechanism and transition in a differentially heated square cavity," J. Fluid Mech. 290, 319–344 (1995).

7S. Paolucci and D. R. Chenoweth, "Transition to chaos in a differentially heated vertical cavity," J. Fluid Mech. 201, 379—410 (1989).

⁸P. L. Quéré and M. Behnia, "From onset of unsteadiness to chaos in a differentially heated square cavity," J. Fluid Mech. 359, 81–107 (1998).

⁹F. X. Trias, A. Gorobets, M. Soria, and A. Oliva, "Direct numerical simulation of a differentially heated cavity of aspect ratio 4 with Rayleigh numbers up to 10¹¹—Part 1: Numerical methods," Int. J. Heat Mass Transfer 53, 665–673 (2010).

¹⁰F. X. Trias, A. Gorobets, M. Soria, and A. Oliva, "Direct numerical simulation of a differentially heated cavity of aspect ratio 4 with Rayleigh numbers up to 10¹¹—Part 2: Heat transfer and flow dynamics," Int. J. Heat Mass Transfer 53, 674–683 (2010).

¹¹X. Wen, L. P. Wang, Z. L. Guo, and D. B. Zhakebayev, "Laminar to turbulent flow transition inside the boundary layer adjacent to isothermal wall of natural convection flow in a cubical cavity," Int. J. Heat Mass Transfer 167, 120822 (2021).

¹²P. Wang, S. Tao, and Z. L. Guo, "A coupled discrete unified gas-kinetic scheme for Boussinesq flows," Comput. Fluids 120, 70–81 (2015).

¹³Z. Chen, C. Shu, and D. Tan, "Three-dimensional simplified and unconditionally stable lattice Boltzmann method for incompressible isothermal and thermal flows," Phys. Fluids 29, 053601 (2017).

¹⁴F. Sebilleau, R. Issa, S. Lardeau, and S. P. Walker, "Direct numerical simulation of an air-filled differentially heated square cavity with Rayleigh number up to 10¹¹," Int. J. Heat Mass Transf. 123, 297–319 (2018).

15 R. J. A. Janssen and R. A. W. M. Henkes, "Instabilities in three-dimensional differentially-heated cavities with adiabatic horizontal walls," Phys. Fluids 8, 62–74 (1996).

¹⁶T. Fusegi, J. M. Hyun, and K. Kuwahara, "Three-dimensional simulations of natural convection in a sidewall-heated cube," Int. J. Numer. Methods Fluids 13, 857–867 (1991).

17 E. Tric, G. Labrosse, and M. Betrouni, "A first incursion into the three-dimensional structure of natural convection of air in a differentially heated cubic cavity, from accurate numerical solutions," Int. J. Heat Mass Transfer 43, 4043–4056 (2000).

¹⁸G. Labrosse, E. Tric, H. Khallouf, and M. Betrouni, "A direct(pseudo-spectral) solver of the two-/three-dimensional stokes problem: Transition to

- unsteadiness of natural-convection flow in a differentially heated cubical cavity," Numer. Heat Transfer 31, 261–276 (1997).
- ¹⁹F. X. Trias, M. Soria, A. Oliva, and C. D. Pérez-Segarra, "Direct numerical simulations of two- and three-dimensional turbulent natural convection flows in a differentially heated cavity of aspect ratio 4," J. Fluid Mech. 586, 259–293 (2007)
- ²⁰S. Paolucci, "On the filtering of sound from the Navier-Stokes equations," Technical Report No. SAND82-8257 (Sandia National Laboratories, 1982).
- ²¹J. Vierendeels, B. Merci, and E. Dick, "Numerical study of natural convective heat transfer with large temperature differences," Int. J. Numer. Method Heat Fluid Flow 11, 329–341 (2001).
- ²²J. Vierendeels, B. Merci, and E. Dick, "Benchmark solutions for the natural convective heat transfer problem in a square cavity with large horizontal temperature differences," Int. J. Numer. Method Heat Fluid Flow 13, 1057–1078 (2003)
- ²³R. Becker and M. Braack, "Solution of a stationary benchmark problem for natural convection with large temperature difference," Int. J. Therm. Sci. 41, 428–439 (2002).
- ²⁴V. Heuveline, "On higher-order mixed FEM for low Mach number flows: Application to a natural convection benchmark problem," Int. J. Numer. Methods Fluids 41, 1339–1356 (2003).
- ²⁵M. Darbandi and S. F. Hosseinizadeh, "Numerical study of natural convection in vertical enclosures using a novel non-Boussinesq algorithm," Numer. Heat Transfer, Part A 52, 849–873 (2007).
- ²⁶Q. Li, K. H. Luo, Y. L. He, and W. Q. Tao, "Coupling lattice Boltzmann model for simulation of thermal flows on standard lattices," Phys. Rev. E 85, 016710 (2012).
- ²⁷D. R. Chenoweth and S. Paolucci, "Natural convection in an enclosed vertical air layer with large horizontal temperature differences," J. Fluid Mech. 169, 173–210 (1986).
- ²⁸P. L. Quéré, R. Masson, and P. Perrot, "A Chebyshev collocation algorithm for 2D non-Boussinesq convection," J. Comput. Phys. 103, 320–335 (1992).
- ²⁹S. Lenz, M. Krafczyk, M. Geier, S. Z. Chen, and Z. L. Guo, "Validation of a two-dimensional gas-kinetic scheme for compressible natural convection on structured and unstructured meshes," Int. J. Therm. Sci. 136, 299–315 (2019).
- 30 X. Wen, L. P. Wang, Z. L. Guo, and J. Shen, "An improved discrete unified gas kinetic scheme for simulating compressible natural convection flows," J. Comput. Phys.: X 11, 100088 (2021).
- 31P. L. Quéré, C. Weisman, H. Paillére, J. Vierendeels, E. Dick, R. Becker, M. Braack, and J. Jocke, "Modeling of natural convection flows with large temperature differences: A benchmark problem for low Mach number solvers. Part 1. Reference solutions," ESAIM: Math. Modell. Numer. Anal. 39, 609–616 (2005).
- ³²H. Paillére, P. L. Quéré, C. Weisman, J. Vierendeels, E. Dick, M. Braack, F. Dabbene, A. Beccantini, E. Studer, T. Kloczko, C. Corre, V. Heuveline, M. Darbandi, and S. F. Hosseinizadeh, "Modeling of natural convection flows with large temperature differences: A benchmark problem for low Mach number solvers. Part 2. Contribution to the June 2004 conference," ESAIM: Math. Modell. Numer. Anal. 39, 617–621 (2005).
- 33Y. L. Feng, P. Sagaut, and W. Q. Tao, "A three dimensional lattice model for thermal compressible flow on standard lattices," J. Comput. Phys. 303, 514 529 (2015)
- 34Y. L. Feng, S. L. Guo, W. Q. Tao, and P. Sagaut, "Regularized thermal lattice Boltzmann method for natural convection with large temperature differences," Int. J. Heat Mass Transfer 125, 1379–1391 (2018).
- 35Q. Wang, S. N. Xia, R. Yan, D. J. Sun, and Z. H. Wan, "Non-Oberbeck-Boussinesq effects due to large temperature differences in a differentially heated square cavity filled with air," Int. J. Heat Mass Transfer 128, 479–491 (2019)
- ³⁶F. J. Alexander, H. Chen, S. Chen, and G. D. Doolen, "Lattice Boltzmann model for compressible fluids," Phys. Rev. A 46, 1967–1970 (1992).

- 37X. Y. He, S. Y. Chen, and G. D. Doolen, "A novel thermal model for the lattice Boltzmann method in incompressible limit," J. Comput. Phys. 146, 282–300 (1998).
- 38 P. Lallemand and L. S. Luo, "Hybrid finite-difference thermal lattice Boltzmann equation," Int. J. Mod. Phys. B 17, 41–47 (2003).
- 39Z. L. Guo, C. Zheng, B. C. Shi, and T. S. Zhao, "Thermal lattice Boltzmann equation for low Mach number flows: Decoupling model," Phys. Rev. E 75, 036704 (2007).
- ⁴⁰A. Scagliarini, L. Biferale, M. Sbragaglia, K. Sugiyama, and F. Toschi, "Lattice Boltzmann methods for thermal flows: Continuum limit and applications to compressible Rayleigh-Taylor systems," Phys. Fluids 22, 055101 (2010).
- ⁴¹T. Chen, X. Wen, L. P. Wang, Z. L. Guo, J. C. Wang, and S. Y. Chen, "Simulation of three-dimensional compressible decaying isotropic turbulence using a redesigned discrete unified gas kinetic scheme," Phys. Fluids 32, 125104 (2020)
- 42H. N. Dixit and V. Babu, "Simulation of high Rayleigh number natural convection in a square cavity using the lattice Boltzmann method," Int. J. Heat Mass Transfer 49, 727–739 (2006).
- ⁴³L. H. Hung and J. Y. Yang, "A coupled lattice Boltzmann model for thermal flows," IMA J. Appl. Math. 76, 774–789 (2011).
- ⁴⁴Z. L. Guo, R. J. Wang, and K. Xu, "Discrete unified gas kinetic scheme for all Knudsen number flow. 2. Thermal compressible case," Phys. Rev. E **91**, 033313 (2015).
- ⁴⁵X. W. Shan, X. F. Yuan, and H. D. Chen, "Kinetic theory representation of hydrodynamics: A way beyond the Navier-Stokes equation," J. Fluid Mech. 550, 413–441 (2006).
- ⁴⁶Z. L. Guo, R. J. Wang, and K. Xu, "Discrete unified gas kinetic scheme for all Knudsen number flow: Low-speed isothermal case," Phys. Rev. E 88, 033305 (2013).
- 47Z. L. Guo and K. Xu, "Discrete unified gas kinetic scheme for multiscale heat transfer based on the phonon Boltzmann transport equation," Int. J. Heat Mass Transfer 102, 944–958 (2016).
- ⁴⁸C. Li and L. P. Wang, "An immersed boundary-discrete unified gas kinetic scheme for simulating natural convection involving curved surface," Int. J. Heat Mass Transfer 126, 1059–1070 (2018).
- ⁴⁹X. Wen, L. P. Wang, and Z. L. Guo, "Designing a consistent implementation of the discrete unified gas-kinetic scheme for the simulation of three-dimensional compressible natural convection," Phys. Fluids 33, 046101 (2021).
- 50T. Chen, X. Wen, L. P. Wang, Z. L. Guo, J. C. Wang, S. Y. Chen, and D. B. Zhakebayev, "Simulation of three-dimensional forced compressible isotropic turbulence by a redesigned discrete unified gas kinetic scheme," J. Comput. Phys. (submitted).
- ⁵¹P. Wang, L. H. Zhu, Z. L. Guo, and K. Xu, "A comparative study of LBE and DUGKS methods for nearly incompressible flows," Commun. Comput. Phys. 17, 657–681 (2015).
- 52Y. T. Bo, P. Wang, Z. L. Guo, and L. P. Wang, "DUGKS simulations of three-dimensional Taylor-Green vortex flow and turbulent channel flow," Comput. Fluids 155, 9–21 (2017).
- ⁵³L. H. Zhu, P. Wang, and Z. L. Guo, "Performance evaluation of the general characteristic based off-lattice Boltzmann scheme and DUGKS for low speed continuum flows," J. Comput. Phys. 333, 227–246 (2017).
- ⁵⁴P. I. Bhatnagar, E. P. Gross, and M. Krook, "A model for collision process in gases. I. Small amplitude processes in charged and neutral one-component systems," Phys. Rev. **94**, 511–525 (1954).
- ⁵⁵E. M. Shakhov, "Generalization of the Krook kinetic relaxation equation," Fluid Dyn. 3, 95–96 (1968).
- 56L. H. Holway, "New statistical model for kinetic theory: Method of construction." Phys. Fluids 9, 1658 (1966).
- ⁵⁷L. Lees, "The stability of the laminar boundary layer in a compressible fluid," NACA Annu. Rep. 33, 331–377 (1947).